7-2018

USE OF A TRIBOELECTRIC GENERATOR FOR A TUNABLE WIDEBAND ENERGY HARVESTER AND A THRESHOLD SHOCK SENSOR

Daniel S. Nelson
Binghamton University--SUNY, dnelson7@binghamton.edu

USE OF A TRIBOELECTRIC GENERATOR FOR A TUNABLE WIDEBAND ENERGY HARVESTER AND A THRESHOLD SHOCK SENSOR

BY

DANIEL NELSON

BS, State University of New York at Geneseo, 2016

THESIS

Submitted in partial fulfillment of the requirements for
the degree of Master of Science in Mechanical Engineering
in the Graduate School of
Binghamton University
State University of New York
2018

Accepted in partial fulfillment of the requirements for
the degree of Master of Science in Mechanical Engineering
in the Graduate School of
Binghamton University
State University of New York
2018

July 27, 2018

Shahrzad Towfighian, Chair (Advisor)
Department of Mechanical Engineering, Binghamton University

Ronald Miles, Member
Department of Mechanical Engineering, Binghamton University

Kaiyan Yu, Member
Department of Mechanical Engineering, Binghamton University

Abstract

The prevalence of triboelectricity as a transduction mechanism has increased rapidly in recent years. We will discuss two uses for triboelectric generators. One design is a tunable wideband energy harvester. An axial force and amplitude limiter work together to create an energy harvester that can accommodate various frequency sources and have a large operating bandwidth. The addition of the compressive axial force also softens the system, which allows for higher voltage outputs. A proof of concept of a threshold shock sensor is proposed that incorporates bi-stability along with the triboelectric effect. A clamped-clamped buckled beam will switch stable states when a threshold shock amplitude is experienced and a voltage peak will occur during this switching of states. Levels of input acceleration can be related to voltage output, which increases the value of the concept. Thorough continuous electro-mechanical models will be produced for each design and the validity of these models will be tested.

Acknowledgements

I would like to thank my girlfriend, Kimmy Giacalone, and my family for all of the help and support they have given me in the past two years. Many thanks go to my advisor, Dr. Shahrzad "Sherry" Towfighian, and Alwathiqbellah Ibrahim for all of the knowledge and guidance they have given me. I have learned more than I could have imagined, and have had a lot of fun doing it. Also, thank you to everyone in the lab for any of the questions they may have answered or tips they may have had to make the research process run more smoothly.

Contents

List of Tables

List of Figures

1 Introduction

1.1 Triboelectric Generators

Energy harvesting at a very basic level is the transfer of energy from an energy source by a transduction mechanism to be used to power devices. An area of interest for researchers is the transfer of mechanical energy to electrical energy. The goal is to use the many sources of ambient vibration that naturally occur to provide power to battery and sensor networks, or to relate a mechanical motion to an electrical output. Some common transduction mechanisms consist of piezoelectricity, electrostatics, electromagnetism, and triboelectricity. We will be focusing on triboelectricity as a transduction mechanism in this discussion. Triboelectricity has many qualities that are more desirable compared to other transduction mechanisms, such as low manufacturing and fabrication costs, high energy densities, and flexibility [1]. When using triboelectric transduction, the system has the capability to be self-sufficient because of the triboelectric effect. The triboelectric effect is the generation of charges due to the contact and separation of certain materials. These triboelectric charges can be retained on the materials for extended periods of time which is useful because many vibration sources are not continuously vibrating all of the time. If the triboelectric materials are attached to metals (electrodes) and a load resistance is inserted between the electrodes, the continuous contact and separation of the triboelectric materials will generate an alternating current through the load. Current will only be generated when there is relative motion between the triboelectric materials, which makes triboelectric transduction a great sensing tool. The following sections will briefly describe the basics of wideband energy harvesting and threshold shock sensing.

1.2 Wideband Energy Harvesting

Traditionally, many energy harvesters can can only be used at a certain frequency and suffer low operating bandwidths. Tunable harvesters are advantageous because for many harvesters, any deviation from the natural frequency dramatically decreases the power output. If the natural frequency of the device can be tuned, then the system can match the source frequency to maximize the power output. Some tunable harvesters can dynamically change, but in doing so, they consume large amounts of power so an external power source is needed. So although it may not be as efficient, being able to statically tune the harvester can result in a system that consumes less power. A common way of statically tuning energy harvesters is by including an axial force to change the natural frequency of the system. This is the method that will be used in this discussion. The inclusion of a compressive axial force will allow the natural frequency to decrease to match a variety of excitation frequencies.

Another drawback to many traditional vibration energy harvesters is that they have low operating bandwidths. Similar to what was previously discussed, a slight change in the source frequency results in a significant drop in power output. Therefore, ways to increase the operating bandwidth of vibration energy harvesters have been explored. Some of the common methods for accomplishing this goal are including a nonlinearity in the system and by using amplitude limiters. The inclusion of a nonlinearity will usually result in a hardening or softening frequency response with larger bandwidths. Common ways to introduce a nonlinearity to a system are by using magnetic forces, geometric nonlinearities such as large deflections of clamped-clamped beams, and nonlinear materials. Another way of increasing operating bandwidths is by limiting the displacement amplitude of the system in some way. Usually the impact that occurs because of the amplitude limiter is related to the power output, so if impacts can occur at frequencies far away from the natural frequency, larger power bandwidths can be experienced.

To have the ability to tune the system and to increase the operating band-

width, we will propose a tunable wideband energy harvester using triboelectric transduction. The system will be tuned by adding a compressive axial force which will allow the system to accommodate different low frequency sources. The addition of the axial force will also soften the system which will result in higher voltage and power outputs. We will be using the inherent impact that occurs due to the triboelectric effect to increase the operating bandwidth. As the impact results in larger voltage outputs, we will be using the impact as an amplitude limiter to extend the bandwidth.

1.3 Threshold Shock Sensor

Many threshold sensor designs are mechanical and require the system to be physically checked to determine if the device was triggered. There is usually only an indication that the device was triggered (the threshold acceleration was met), but the actual magnitude of the acceleration is not known. Many systems that combine mechanical and electrical action use electrostatics. The drawback to electrostatics is that the threshold sensors usually rely on the pull in voltage and therefore require a bias voltage, so these sensors cannot be self powered. To avoid using bias voltages, the use of bi-stability is a common approach to designing threshold sensors. This is because in a bi-stable system, there are two stable states. So depending how the bi-stability is incorporated into the system, when the system moves from one stable state to another, it is known that the device was triggered. Buckled clamped-clamped beams are a natural candidate for threshold sensors due to the two stable states that they have.

We will be combining bi-stability with triboelectric transduction to propose a proof of concept of a threshold shock sensor. A triboelectric material will be placed at the midspan of the beam and another triboelectric material will be placed near the lower stable position so that when the beam is in the upper stable position, there is no relative motion between the materials and they are not in contact with each other. When the device senses an acceleration above the

threshold acceleration, the beam will change states and the triboelectric materials will impact each other which will result in a voltage spike. As the level of impact is correlated to the magnitude of the voltage spike, the system will behave like an accelerometer in the region past the threshold acceleration. Combining all of these factors together results in a proof of concept for a self powered threshold sensor.

2 Tunable Wideband Energy Harvester

2.1 Introduction

The major source for powering small electronics is through batteries. However, the limited lifespan, detrimental environmental effects, and high replacement costs are the major drawbacks. Mechanical vibration is considered the most widespread source for harvesting energy that can be found in transportation vehicles and the environment. The need to power small electronics and sensors through harvesting energy from ambient vibrations has driven many research efforts in the recent years [2–4]. To maximize the amount of energy transferred from ambient vibrations to the devices, the natural frequency of these devices should match the excitation frequency from the ambient source. Because of the lower bandwidth of the linear harvesters compared to the higher bandwidth of the ambient vibrations, linear energy harvesters are considered inefficient. To overcome this limitation, several studies have demonstrated the benefits of nonlinearities to improve the bandwidth of the harvesters compared to the linear harvesters [5]. Introducing nonlinearities in the design of energy harvesters are considered promising to broaden the frequency bandwidth. The most common types of nonlinearities for energy harvesting consist of magnetic [6, 7], mechanical forces [8, 9], internal resonances [10, 11], and mechanical stoppers or impacts [12–14].

When the fundamental frequency of the energy harvesters mismatch the excitation frequency even with a small deviation, the amount of energy harvested decreases and the efficiency of the harvester drops. Accordingly, the need for new energy harvester designs with the capability to tune the resonant frequency has become an important topic. Different research studies addressed this point through closed-loop techniques [15, 16], and external power sources [7, 17]. One of the most used

approaches for frequency tuning is the addition of an axial load, where an axial static load can be applied to the harvester structure to change its natural frequency [18, 19]. It was found by Lesieutre and Davis [20] that compressive axial preloads can increase the coupling coefficient of an electrically driven piezoelectric bimorph for a higher output. Leland and Wright [18] were able to tune the natural frequencies of a piezoelectric bimorph simply supported beam with center mass energy harvester through applying a compressive axial preload to soften the beam. The natural frequencies were reduced by 20%. Roundy and Zhang [15] examined the use of electrical feedback to tune the resonance frequency of a piezoelectric bimorph. A continuous actuation is needed to adjust the device periodically to tune its resonance frequency. Other ways to tune the bimorph frequency includes changing the beam length or the attached mass to control the beam stiffness. Masana and Daqaq [8] developed and experimentally validated a nonlinear electromechanical model of a clamped-clamped tunable piezoelectric energy harvester subjected to transversal excitations and static axial loading. With the axial load, they were able to achieve 65% change in the natural frequency. Increasing the axial force resulted in higher output energy and bandwidth due to the increase in the electrical damping, oscillation amplitudes, and structural nonlinearity.

Energy that is converted from a mechanical form into an electrical form use different types of transduction mechanisms such as electromagnetic, electrostatic, and piezoelectric [21–23]. Though piezoelectric generators have been very popular for energy harvesting, their charge density falls behind triboelectric generators [24, 25]. Triboelectric transduction generates power from the periodic contact and separation between two materials with different tendencies to lose and gain electrons. Compared to piezoelectric energy harvesters, triboelectric energy harvesters have the advantages of low manufacturing and fabrication costs, high energy densities, and flexibility [1]. Because of the inherent contact and separation property of triboelectric generators, they have been used for energy harvesting from im-

pact [12, 13]. With a piecewise impact model and experimental validation, they reported higher bandwidths as well as output voltages.

To create tunability and to increase output, we introduce the compressive load to our previously presented impact harvester [12]. The axial force allows the system to be tuned to accommodate various vibration sources. A wider frequency bandwidth is experienced using impact between triboelectric layers. The result is an energy harvester with widened frequency bandwidth spread at low frequencies, which enhances the energy harvesting conversion efficiency because often ambient vibrations have a wide spectrum at low frequencies. To capture a reasonable approximation of the dynamic response of the harvester as well as output, we present a linear continuous model of the electromechanical system. To derive the equations of motion, we use the Extended Hamilton's Principle for linear Euler-Bernoulli beams and Galerkin's decomposition. The model provides a platform for designing high-performance energy harvesters with wide tunable frequency ranges spread at low frequencies.

The outline of this chapter is as follows. The principle of operation will be discussed and a continuous model with be derived in great detail. Then numerical simulations will be performed with the addition of the axial force to determine how the system responds to different axial forces, electrode gaps, and load resistances. The chapter will end with concluding remarks.

2.2 Nomenclature

Table 1: Nomenclature for Chapter 2

Parameter	Description
A_{amp}	Excitation amplitude
A_p	Cross-sectional area of polymer beam
b_m	Width of center mass and upper electrode
B_i, s_i	Constants for mode shape analysis
c, c_i	Damping, impact damping
d_0	Initial total electrode gap
D_1	Damping term from ROM
D_a, D_b	Axial stiffness term, flexural rigidity for second beam span
$D(x)$	Function for flexural rigidity along the beam
E, E_a, E_p	Modulus of elasticity in general, for aluminum, for polymer
E_{air}, E_{PDMS}	Electric field in the air gap, PDMS layer
$F(x)$	Function for axial stiffness term along the beam
F_i, F_d	Impact stiffness and damping forces
g	Acceleration due to gravity
h, h_m	Thickness of the polymer beam, center mass and upper electrode
I	Current through load resistance
I_p	Moment of inertia of polymer beam
k_i, K_L, K_C	Impact, linear, and cubic stiffness coefficients
L	Length of beam
L_1	Location of midspan
L_L	Beginning position of center mass and upper electrode
L_R	Ending position of center mass and upper electrode
$m(x)$	Function for mass per unit length along the beam
M_1, M_Z	Mass coefficient, base acceleration coefficient
p	Compressive axial force
P	Power
$q(t)$	Charge transferred through the load resistance

Continued on next page

Table 1 – *Continued from previous page*

Parameter	**Description**
R	Load resistance
S	Contact area
T	Kinetic energy
T_{PDMS}	Thickness of PDMS layer
$u(x,t)$	Longitudinal deflection of the beam
U	Potential energy
V	Voltage across the load resistance
$w(x,t)$	Absolute transverse deflection of the beam
W_{nc}	Work done by nonconservative forces
$y(x,t)$	Relative transverse deflection of the beam
y_c	Coordinate for the y-axis
$z(t)$	Base motion
z_c	Coordinate for the transverse direction
$\alpha_{a,b}, \beta_{a,b}$	Constants for mode shape analysis
$\alpha_{1,2}$	Electromechanical coupling terms
$\gamma_i(t), \eta(t)$	Arbitrary functions of time
δ	Penetration distance
$\varepsilon, \varepsilon_0, \varepsilon_r$	Permittivity, vacuum permittivity, relative permittivity
$\varepsilon_t, \varepsilon_s$	Total mechanical strain, strain due to mid-plane stretching
ρ_p, ρ_a	Density of polymer beam, aluminum
ρA	Mass per unit length of second span of beam
σ	Surface charge density
σ_t	Mechanical stress
$\phi(x)$	Mode shape
ω, Ω	Natural frequency, excitation frequency

2.3 Principle of Operation

A solid model and a schematic of the system is shown in Fig. 1. The compressive axial force at the ends of the beam will be tuned to change the system's response and dynamics. Although we are using a compressive axial force in this system, we will be controlling the axial force to be less than the critical axial load. Therefore, the beam will not buckle, but instead the axial force provides a softening effect on the system.

Concerning the principle of operation of the triboelectric generator, we have an aluminum mold (upper electrode) and a PDMS layer attached to an aluminum mass (lower electrode). The two electrodes are connected with a load resistance, and the voltage across the load will be measured. When the upper electrode and PDMS layer are initially brought in contact with each other, they will generate triboelectric charges on their surfaces due to the triboelectric effect. When there is relative motion between the electrodes, an electric potential difference will be established and charges will be transferred between the electrodes that results in a generated current. When the upper electrode is at its maximum absolute displacement, there will be an equilibrium of charge, and the electric potential difference will be zero.

The system will be subjected to a harmonic base excitation, which will allow the upper and lower electrodes to periodically impact each other at certain frequencies. At frequencies where an impact does not occur, the upper and lower electrodes will effectively behave as a variable capacitor system. We add an additional mass to the midspan of the beam to increase the inertial force, which will result in a higher velocity and impact force for the upper electrode and a higher voltage output.

2.4 Mathematical Modeling

To improve the accuracy over the lumped parameter system that was done previously [12], a continuous model will be produced for the electromechanical governing

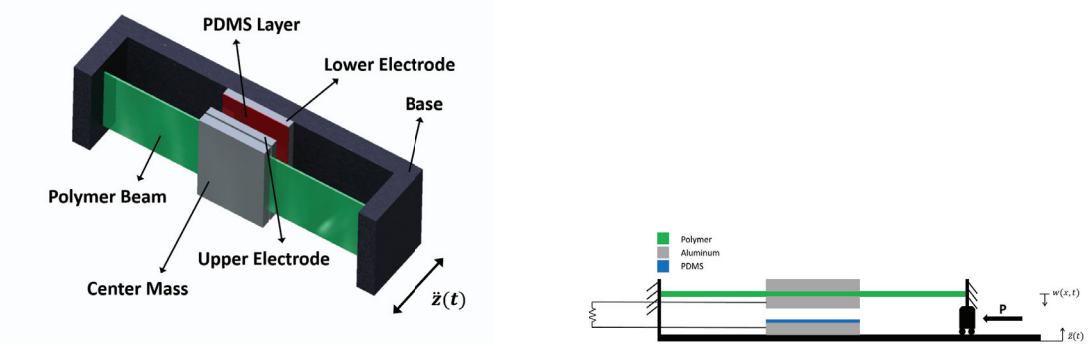

(a) (b)

Figure 1: 3D model and schematic of the system. Some dimensions are exaggerated in order to create a better visual understanding of the system. (a) A 3D model of the system. (b) A schematic of the system.

equations using linear Euler-Bernoulli beam theory. The higher degree of accuracy and the addition of the compressive axial force make it advantageous to develop a continuous model. As we will be limiting the gap between the upper electrode and the PDMS layer to relatively small distances, we will be neglecting any nonlinear effects that would have arisen from mid-plane stretching.

In order to develop our equations of motion we first describe our system. We will be modeling our system as a three span beam, with the first and third spans being the polymer beam, and the second span being a three layer beam consisting of two aluminum layers and a polymer layer. We initially represent the system in terms of the absolute defection of the beam and the base motion.

2.4.1 Deriving Equations of Motion

The equations of motion are derived using the Extended Hamilton's Principle. Its kinetic and potential energy terms are written as

$$T = \frac{1}{2}\rho_p A_p \int_0^{L_L} \dot{w}_1^2 dx + \frac{1}{2}\rho A \int_{L_L}^{L_R} \dot{w}_2^2 dx + \frac{1}{2}\rho_p A_p \int_{L_R}^{L} \dot{w}_3^2 dx \tag{1}$$

where $\rho A = \rho_a b_m h_m + \rho_p A_p + \rho_a b_m h_m$. The potential energy of the system is

$$U = \frac{1}{2}\int_V \varepsilon_s \sigma_s dV + \frac{\varepsilon_0}{2}\int_V E_{air}^2 dV + \frac{\varepsilon_0 \varepsilon_r}{2}\int_V E_{PDMS}^2 dV \tag{2}$$

where

$$\begin{aligned}
\varepsilon_{t_i} &= u_i' + \frac{1}{2}w_i'^2 - z_c w_i'' \\
&= \varepsilon_{s_i} - z_c w_i'' \\
\sigma_{t_i} &= E\varepsilon_{t_i} \\
E_{air} &= \frac{(-q + \sigma S)}{\varepsilon_0 S} \\
E_{PDMS} &= -\frac{q}{\varepsilon_0 \varepsilon_r S}
\end{aligned} \tag{3}$$

Expanding the potential energy expression using Eq. (3), results in

$$
\begin{aligned}
U = & \frac{1}{2}E_p \int_{-b/2}^{b/2} dy_c \int_{-h/2}^{h/2} dz_c \int_0^{L_L} \varepsilon_{s_1}^2 dx + \frac{1}{2}E_p \int_{-b/2}^{b/2} dy_c \int_{-h/2}^{h/2} z_c^2 dz_c \int_0^{L_L} w_1''^2 dx \\
& - E_p \int_{-b/2}^{b/2} dy_c \int_{-h/2}^{h/2} z_c dz_c \int_0^{L_L} \varepsilon_{s_1} w_1'' dx \\
& + \frac{1}{2}E_p \int_{-b/2}^{b/2} dy_c \int_{-h/2}^{h/2} dz_c \int_{L_L}^{L_R} \varepsilon_{s_2}^2 dx + \frac{1}{2}E_p \int_{-b/2}^{b/2} dy_c \int_{-h/2}^{h/2} z_c^2 dz_c \int_{L_L}^{L_R} w_2''^2 dx \\
& - E_p \int_{-b/2}^{b/2} dy_c \int_{-h/2}^{h/2} z_c dz_c \int_{L_L}^{L_R} \varepsilon_{s_2} w_2'' dx \\
& + \frac{1}{2}E_a \int_{-b_m/2}^{b_m/2} dy_c \int_{-h_m-h/2}^{-h/2} dz_c \int_{L_L}^{L_R} \varepsilon_{s_2}^2 dx \\
& + \frac{1}{2}E_a \int_{-b_m/2}^{b_m/2} dy_c \int_{-h_m-h/2}^{-h/2} z_c^2 dz_c \int_{L_L}^{L_R} w_2''^2 dx \\
& - E_a \int_{-b_m/2}^{b_m/2} dy_c \int_{-h_m-h/2}^{-h/2} z_c dz_c \int_{L_L}^{L_R} \varepsilon_{s_2} w_2'' dx \\
& + \frac{1}{2}E_a \int_{-b_m/2}^{b_m/2} dy_c \int_{h/2}^{h_m+h/2} dz_c \int_{L_L}^{L_R} \varepsilon_{s_2}^2 dx \\
& + \frac{1}{2}E_a \int_{-b_m/2}^{b_m/2} dy_c \int_{h/2}^{h_m+h/2} z_c^2 dz_c \int_{L_L}^{L_R} w_2''^2 dx \\
& - E_a \int_{-b_m/2}^{b_m/2} dy_c \int_{h/2}^{h_m+h/2} z_c dz_c \int_{L_L}^{L_R} \varepsilon_{s_2} w_2'' dx \\
& + \frac{1}{2}E_p \int_{-b/2}^{b/2} dy_c \int_{-h/2}^{h/2} dz_c \int_{L_R}^{L} \varepsilon_{s_3}^2 dx + \frac{1}{2}E_p \int_{-b/2}^{b/2} dy_c \int_{-h/2}^{h/2} z_c^2 dz_c \int_{L_R}^{L} w_3''^2 dx \\
& - E_p \int_{-b/2}^{b/2} dy_c \int_{-h/2}^{h/2} z_c dz_c \int_{L_R}^{L} \varepsilon_{s_3} w_3'' dx \\
& + \frac{\varepsilon_0 \varepsilon_r}{2} \int_{-b_m/2}^{b_m/2} dy_c \int_{L_L}^{L_R} dx \int_{d_0-T_{PDMS}}^{d_0} \frac{q^2}{\varepsilon_0^2 \varepsilon_r^2 S^2} dz_c \\
& + \frac{\varepsilon_0}{2} \int_{-b_m/2}^{b_m/2} dy_c \int_{L_L}^{L_R} dx \int_{w_2(L_1)-z(t)}^{d_0} \Big(\frac{q^2}{\varepsilon_0^2 S^2} + \frac{\sigma^2}{\varepsilon_0^2} - \frac{2q\sigma}{\varepsilon_0^2 S} \Big) dz_c
\end{aligned}
\tag{4}
$$

Because we are assuming the neutral axis of the beam is the centerline of the beam the integrals ($\int z_c dz_c$) will drop out of Eq. (4). We further simplify Eq. (4) to get

$$
\begin{aligned}
U = & \frac{1}{2}E_pA_p\int_0^{L_L}\varepsilon_{s_1}^2dx + \frac{1}{2}E_pI_p\int_0^{L_L}w_1''^2dx + \frac{1}{2}D_a\int_{L_L}^{L_R}\varepsilon_{s_2}^2dx \\
& + \frac{1}{2}D_b\int_{L_L}^{L_R}w_2''^2dx + \frac{1}{2}E_pA_p\int_{L_R}^{L}\varepsilon_{s_3}^2dx + \frac{1}{2}E_pI_p\int_{L_R}^{L}w_3''^2dx \\
& + \frac{T_{PDMS}}{2\varepsilon_0\varepsilon_r S}q^2 + \frac{d_0 - w_2(L_1) + z(t)}{2\varepsilon_0 S}q^2 - \frac{\sigma\Big(d_0 - w_2(L_1) + z(t)\Big)}{\varepsilon_0}q \\
& + \frac{\sigma^2 S\Big(d_0 - w_2(L_1) + z(t)\Big)}{2\varepsilon_0}
\end{aligned}
\tag{5}
$$

where

$$
\begin{aligned}
D_a &= E_a h_m b_m + E_p A_p + E_a h_m b_m \\
D_b &= E_a b_m\Big(\frac{h_m^3}{3} + \frac{hh_m^2}{2} + \frac{h^2h_m}{4}\Big) + E_pI_p + E_a b_m\Big(\frac{h_m^3}{3} + \frac{hh_m^2}{2} + \frac{h^2h_m}{4}\Big)
\end{aligned}
\tag{6}
$$

The variation of the work due to the nonconservative forces is

$$
\delta W_{nc} = -c\int_0^{L_L}\dot{w}_1\delta w_1 dx - c\int_{L_L}^{L_R}\dot{w}_2\delta w_2 dx - c\int_{L_R}^{L}\dot{w}_3\delta w_3 dx - R\dot{q}\delta q - p\delta w_3(L) \tag{7}
$$

Let $w_i(x,t) = y_i(x,t) + z(t)$, derive the variations of the kinetic and potential energies.

$$
\delta T = \rho_p A_p\int_0^{L_L}\dot{w}_1\delta\dot{w}_1 dx + \rho A\int_{L_L}^{L_R}\dot{w}_2\delta\dot{w}_2 dx + \rho_p A_p\int_{L_R}^{L}\dot{w}_3\delta\dot{w}_3 dx \tag{8}
$$

$$
\begin{aligned}
\delta U = {} & E_p A_p \int_0^{L_L} \varepsilon_{s_1} \delta u_1' dx + E_p A_p \int_0^{L_L} \varepsilon_{s_1} w_1' \delta w_1' dx + E_p I_p \int_0^{L_L} w_1'' \delta w_1'' dx \\
& + D_a \int_{L_L}^{L_R} \varepsilon_{s_2} \delta u_2' dx + D_a \int_{L_L}^{L_R} \varepsilon_{s_2} w_2' \delta w_2' dx + D_b \int_{L_L}^{L_R} w_2'' \delta w_2'' dx \\
& + E_p A_p \int_{L_R}^{L} \varepsilon_{s_3} \delta u_3' dx + E_p A_p \int_{L_R}^{L} \varepsilon_{s_3} w_3' \delta w_3' dx + E_p I_p \int_{L_R}^{L} w_3'' \delta w_3'' dx \\
& + \frac{T_{PDMS}}{\varepsilon_0 \varepsilon_r S} q \delta q + \frac{d_0 - y_2(L_1)}{\varepsilon_0 S} q \delta q - \frac{q^2}{2\varepsilon_0 S} \delta y_2(L_1) - \frac{\sigma\Big(d_0 - y_2(L_1)\Big)}{\varepsilon_0} \delta q \\
& + \frac{\sigma q}{\varepsilon_0} \delta y_2(L_1) - \frac{\sigma^2 S}{2\varepsilon_0} \delta y_2(L_1)
\end{aligned} \tag{9}
$$

The Extended Hamilton's Principle is now used, $\int_{t_1}^{t_2} (\delta T - \delta U + \delta W_{nc}) dt = 0$.

$$
\begin{aligned}
\int_{t_1}^{t_2} \delta T dt = {} & \int_0^{L_L} \Big[\rho_p A_p \Big(\dot{y}_1 + \dot{z} \Big) \delta y_1 \Big|_{t_1}^{t_2} - \int_{t_1}^{t_2} \rho_p A_p \Big(\ddot{y}_1 + \ddot{z} \Big) \delta y_1 dt \Big] dx \\
& + \int_{L_L}^{L_R} \Big[\rho A \Big(\dot{y}_2 + \dot{z} \Big) \delta y_2 \Big|_{t_1}^{t_2} - \int_{t_1}^{t_2} \rho A \Big(\ddot{y}_2 + \ddot{z} \Big) \delta y_2 dt \Big] dx \\
& + \int_{L_R}^{L} \Big[\rho_p A_p \Big(\dot{y}_3 + \dot{z} \Big) \delta y_3 \Big|_{t_1}^{t_2} - \int_{t_1}^{t_2} \rho_p A_p \Big(\ddot{y}_3 + \ddot{z} \Big) \delta y_3 dt \Big] dx
\end{aligned} \tag{10}
$$

By using the definition of virtual work, we simplify Eq. (10).

$$
\begin{aligned}
\int_{t_1}^{t_2} \delta T dt = \int_{t_1}^{t_2} \Bigg[& - \int_0^{L_L} \rho_p A_p \Big(\ddot{y}_1 + \ddot{z} \Big) \delta y_1 dx - \int_{L_L}^{L_R} \rho A \Big(\ddot{y}_2 + \ddot{z} \Big) \delta y_2 dx \\
& - \int_{L_R}^{L} \rho_p A_p \Big(\ddot{y}_3 + \ddot{z} \Big) \delta y_3 dx \Bigg] dt
\end{aligned} \tag{11}
$$

Moving on to the next part, we have

$$
\begin{aligned}
\int_{t_1}^{t_2} \delta U dt = \int_{t_1}^{t_2} \Bigg[& E_p I_p y_1'' \delta y_1' \Big|_0^{L_L} - E_p I_p y_1''' \delta y_1 \Big|_0^{L_L} + E_p I_p \int_0^{L_L} y_1'''' \delta y_1 dx \\
& + D_b y_2'' \delta y_2' \Big|_{L_L}^{L_R} - D_b y_2''' \delta y_2 \Big|_{L_L}^{L_R} + D_b \int_{L_L}^{L_R} y_2'''' \delta y_2 dx \\
& + E_p I_p y_3'' \delta y_3' \Big|_{L_R}^{L} - E_p I_p y_3''' \delta y_3 \Big|_{L_R}^{L} + E_p I_p \int_{L_R}^{L} y_3'''' \delta y_3 dx \\
& + E_p A_p \varepsilon_{s_1} \delta u_1 \Big|_0^{L_L} - E_p A_p \int_0^{L_L} \varepsilon_{s_1}' \delta u_1 dx \\
& + E_p A_p \varepsilon_{s_1} y_1' \delta y_1 \Big|_0^{L_L} - E_p A_p \int_0^{L_L} \Big[\varepsilon_{s_1} y_1' \Big]' \delta y_1 dx \\
& + D_a \varepsilon_{s_2} \delta u_2 \Big|_{L_L}^{L_R} - D_a \int_{L_L}^{L_R} \varepsilon_{s_2}' \delta u_2 dx \\
& + D_a \varepsilon_{s_2} y_2' \delta y_2 \Big|_{L_L}^{L_R} - D_a \int_{L_L}^{L_R} \Big[\varepsilon_{s_2} y_2' \Big]' \delta y_2 dx \\
& + E_p A_p \varepsilon_{s_3} \delta u_3 \Big|_{L_R}^{L} - E_p A_p \int_{L_R}^{L} \varepsilon_{s_3}' \delta u_3 dx \\
& + E_p A_p \varepsilon_{s_3} y_3' \delta y_3 \Big|_{L_R}^{L} - E_p A_p \int_{L_R}^{L} \Big[\varepsilon_{s_3} y_3' \Big]' \delta y_3 dx \\
& + \frac{T_{PDMS}}{\varepsilon_0 \varepsilon_r S} q \delta q + \frac{d_0 - y_2(L_1)}{\varepsilon_0 S} q \delta q - \frac{q^2}{2\varepsilon_0 S} \delta y_2(L_1) - \frac{\sigma \Big(d_0 - y_2(L_1) \Big)}{\varepsilon_0} \delta q \\
& + \frac{\sigma q}{\varepsilon_0} \delta y_2(L_1) - \frac{\sigma^2 S}{2\varepsilon_0} \delta y_2(L_1) \Bigg] dt
\end{aligned}
\tag{12}
$$

The governing equations and boundary conditions for the transverse direction, longitudinal direction, and charge are determined. The equations for the longitudinal and transverse directions are first considered.

$$\begin{cases} E_p A_p \varepsilon'_{s_1} = 0 & 0 \le x \le L_L \\ E_p I_p y_1'''' + \rho_p A_p \ddot{y}_1 + \rho_p A_p \ddot{z} + c\dot{y}_1 - E_p A_p (\varepsilon_{s_1} y'_1)' = 0 & 0 \le x \le L_L \\ D_a \varepsilon'_{s_2} = 0 & L_L \le x \le L_R \\ D_b y_2'''' + \rho A \ddot{y}_2 + \rho A \ddot{z} + c\dot{y}_2 - D_a (\varepsilon_{s_2} y'_2)' = 0 & L_L \le x \le L_R \\ E_p A_p \varepsilon'_{s_3} = 0 & L_R \le x \le L \\ E_p I_p y_3'''' + \rho_p A_p \ddot{y}_3 + \rho_p A_p \ddot{z} + c\dot{y}_3 - E_p A_p (\varepsilon_{s_3} y'_3)' = 0 & L_R \le x \le L \end{cases} \tag{13}$$

As the mechanical strain is mostly in the longitudinal direction due to limited transverse deflections, we will be making the approximation that $\varepsilon_{s_i} \approx u'_i$. We now attempt to decouple the longitudinal and transverse equations of motion. The equations of motion and boundary conditions will be

$$\begin{aligned} u_1(x) &= \gamma_1(t)x + \gamma_2(t) \\ u_2(x) &= \gamma_3(t)(x - L_L) + \gamma_4(t) \\ u_3(x) &= \gamma_5(t)(x - L_R) + \gamma_6(t) \\ u_1(0) &= 0 \\ u_1(L_L) &= u_2(L_L) \\ u_2(L_R) &= u_3(L_R) \\ u_1(L_L) &= -\frac{pL_L}{E_p A_p} \\ u_2(L_R) &= \frac{pL_L}{D_a} - \frac{pL_L}{E_p A_p} - \frac{pL_R}{D_a} \\ u_3(L) &= -\frac{pL}{E_p A_p} + \frac{pL_L}{D_a} - \frac{pL_L}{E_p A_p} - \frac{pL_R}{D_a} + \frac{pL_R}{E_p A_p} \end{aligned} \tag{14}$$

It can be shown that

$$\begin{aligned} \varepsilon_{s_1} &= \varepsilon_{s_3} = \gamma_1(t) = \gamma_5(t) = -\frac{p}{E_p A_p} \\ \varepsilon_{s_2} &= \gamma_3(t) = -\frac{p}{D_a} \end{aligned} \tag{15}$$

We have now successfully decoupled the longitudinal and transverse equations of motion. We can now fully represent the transverse equations of motion along with the corresponding boundary conditions. The physical boundary conditions are determined from the clamped edges. We use the fact that since we effectively have a large plate in the center of the beam, the position at $x = L_L$, $x = L_1$, and $x = L_R$ is the same, and the slope is zero at $x = L_L$ and $x = L_R$. The remaining boundary condition is determined from Hamilton's Principle, as well as the governing equation for the charge.

$$
\begin{cases}
E_pI_py_1'''' + \rho_pA_p\ddot{y}_1 + \rho_pA_p\ddot{z} + c\dot{y}_1 + py_1'' = 0 & 0 \le x \le L_L \\
D_by_2'''' + \rho A\ddot{y}_2 + \rho A\ddot{z} + c\dot{y}_2 + py_2'' = 0 & L_L \le x \le L_R \\
E_pI_py_3'''' + \rho_pA_p\ddot{y}_3 + \rho_pA_p\ddot{z} + c\dot{y}_3 + py_3'' = 0 & L_R \le x \le L \\
\dot{q} = \frac{-q}{\varepsilon_0 RS}\left[\frac{T_{PDMS}}{\varepsilon_r} + d_0 - y_2(L_1)\right] + \frac{\sigma(d_0 - y_2(L_1))}{\varepsilon_0 R} & \\
y_1(0,t) = 0 & \\
y_1'(0,t) = 0 & \\
y_3(L,t) = 0 & \\
y_3'(L,t) = 0 & \\
y_1(L_L,t) = y_2(L_L,t) & \\
y_2(L_R,t) = y_3(L_R,t) & \\
y_2(L_L,t) = y_2(L_R,t) & \\
y_1'(L_L,t) = 0 & \\
y_2'(L_L,t) = 0 & \\
y_2'(L_R,t) = 0 & \\
y_3'(L_R,t) = 0 & \\
E_pI_py_1'''(L_L,t) + D_by_2''''(L_R,t) - D_by_2''''(L_L,t) & \\
\qquad -E_pI_py_3'''(L_R,t) + \frac{q^2}{2\varepsilon_0 S} - \frac{\sigma q}{\varepsilon_0} + \frac{\sigma^2 S}{2\varepsilon_0} = 0 &
\end{cases}
\tag{16}
$$

2.4.2 Determine Mode Shapes

We will now determine the mode shape and natural frequency of the system around the static configuration. The static configuration will be the trivial solution as we let the transverse motion be perpendicular to the force of gravity. Therefore there will be negligible gravitational effect on the static configuration. Since we are concerned with the vibrations around the trivial static configuration, we let

$$y_i(x,t) = \phi_i(x)e^{j\omega t} \tag{17}$$

The i subscript for the mode shape denotes the span, not the mode number, as we will only be considering a first mode approximation. Substituting Eq. (17) into Eq. (16) and neglecting the damping, forcing, and electrical terms yield

$$\begin{cases} -\rho_p A_p \omega^2 \phi_1 + E_p I_p \phi_1'''' + p\phi_1'' = 0 & 0 \le x \le L_L \\ -\rho A \omega^2 \phi_2 + D_b \phi_2'''' + p\phi_2'' = 0 & L_L \le x \le L_R \\ -\rho_p A_p \omega^2 \phi_3 + E_p I_p \phi_3'''' + p\phi_3'' = 0 & L_R \le x \le L \end{cases} \tag{18}$$

Let $\alpha_a = \frac{p}{E_p I_p}$, $\beta_a = \frac{\rho_p A_p \omega^2}{E_p I_p}$, $\alpha_b = \frac{p}{D_b}$, and $\beta_b = \frac{\rho A \omega^2}{D_b}$ and assume trial functions $\phi_i(x)$ are

$$\begin{aligned} \phi_{1,3}(x) &= B_1 \cosh(s_1 x) + B_2 \sinh(s_1 x) + B_3 \cos(s_2 x) + B_4 \sin(s_2 x) \\ \phi_2(x) &= B_1 \cosh(s_3 x) + B_2 \sinh(s_3 x) + B_3 \cos(s_4 x) + B_4 \sin(s_4 x) \end{aligned} \tag{19}$$

where $s_{1,2} = \sqrt{\frac{\mp\alpha_a + \sqrt{\alpha_a^2 + 4\beta_a}}{2}}$ and $s_{3,4} = \sqrt{\frac{\mp\alpha_b + \sqrt{\alpha_b^2 + 4\beta_b}}{2}}$. As we can see from Fig. 2, the mode shape provides a reasonable approximation to the physical system that we have, with the polymer beam for the first and third spans and the stiff three layer beam for the second span.

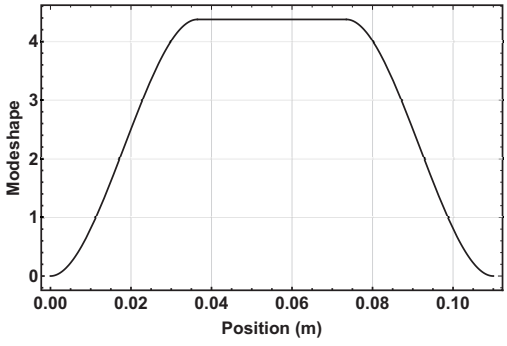

Figure 2: Mode shape of the three span beam with no compressive axial force.

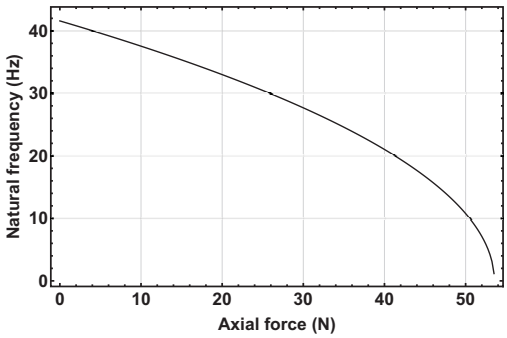

Figure 3: Effect of axial force on the fundamental natural frequency of the system.

The effect of the compressive axial force on the natural frequency is shown in Fig. 3. Before the critical buckling load is reached, the fundamental natural frequency of the system decreases with an increase of axial force. The natural frequency will theoretically approach zero as the axial force approaches the critical buckling axial load. The critical axial load for this system, as observed from Fig. 3, is approximately $52N$.

2.5 Reduced Order Model

To study the dynamics of the system, we develop a Reduced Order Model. Now that the mode shape of the system has been determined, we will be denoting the first mode shape of the system as $\phi(x)$ and will not be including the span notation anymore. Therefore we define the mass per unit length, flexural rigidity, and axial

stiffness terms of the system as functions of the longitudinal coordinate.

$$
\begin{aligned}
m(x) &= \begin{cases} \rho_p A_p & 0 \le x \le L_L \\ \rho A & L_L \le x \le L_R \\ \rho_p A_p & L_R \le x \le L \end{cases} \\
D(x) &= \begin{cases} E_p I_p & 0 \le x \le L_L \\ D_b & L_L \le x \le L_R \\ E_p I_p & L_R \le x \le L \end{cases} \\
F(x) &= \begin{cases} E_p A_p & 0 \le x \le L_L \\ D_a & L_L \le x \le L_R \\ E_p A_p & L_R \le x \le L \end{cases}
\end{aligned} \tag{20}
$$

We determine the Lagrangian of the system ($\mathcal{L} = T - U$), and use Lagrange's Equations to determine the equations for the Reduced Order Model. We will again be using $\varepsilon_s = -\frac{p}{F(x)} + \frac{y'^2}{2}$ in order to determine the Reduced Order Model, but we will be neglecting the cubic terms due to small deformations in the transverse direction of motion. The Lagrangian is defined by

$$
\begin{aligned}
\mathcal{L} = &\frac{1}{2} m(x) \int_0^L (\dot{y} + \dot{z})^2 dx - \frac{1}{2} D(x) \int_0^L y''^2 dx \\
&- \frac{1}{2} F(x) \int_0^L \Big[- \frac{p}{F(x)} + \frac{1}{2} y'^2 \Big]^2 dx - \frac{T_{PDMS}}{2\varepsilon_0 \varepsilon_r S} q^2 \\
&- \frac{d_0 - y(L_1)}{2\varepsilon_0 S} q^2 + \frac{\sigma(d_0 - y(L_1))}{\varepsilon_0} q - \frac{\sigma^2 S (d_0 - y(L_1))}{2\varepsilon_0}
\end{aligned} \tag{21}
$$

To approximate the dynamic deflection of the beam about its trivial static configuration, we use a one mode approximation and let

$$
y(x,t) = \phi(x)\eta(t) \tag{22}
$$

We substitute Eq. (22) into Eq. (21) and perform Lagrange's Equation for the variables $\eta(t)$ and $q(t)$.

$$\frac{d}{dt}\frac{\partial \mathcal{L}}{\partial \dot{\eta}} = m(x)\int_0^L \Big(\phi(x)\ddot{\eta} + \ddot{z}\Big)\phi(x)dx \tag{23}$$

$$\begin{aligned}\frac{\partial \mathcal{L}}{\partial \eta} = &-D(x)\int_0^L \phi''(x)\eta\phi''(x)dx + p\int_0^L \phi'(x)\eta\phi'(x)dx \\ &+ \frac{\phi(L_1)}{2\varepsilon_0 S}q^2 - \frac{\sigma\phi(L_1)}{\varepsilon_0}q + \frac{\sigma^2 S\phi(L_1)}{2\varepsilon_0}\end{aligned} \tag{24}$$

$$\frac{d}{dt}\frac{\partial \mathcal{L}}{\partial \dot{q}} = 0 \tag{25}$$

$$\frac{\partial \mathcal{L}}{\partial q} = -\frac{T_{PDMS}}{\varepsilon_0\varepsilon_r S}q - \frac{d_0 - \phi(L_1)\eta}{\varepsilon_0 S}q + \frac{\sigma\Big(d_0 - \phi(L_1)\eta\Big)}{\varepsilon_0} \tag{26}$$

Using Lagrange's Equation

$$\begin{aligned}\frac{d}{dt}\frac{\partial \mathcal{L}}{\partial \dot{\eta}} - \frac{\partial \mathcal{L}}{\partial \eta} &= -c\int_0^L \phi^2(x)\dot{\eta}dx \\ \frac{d}{dt}\frac{\partial \mathcal{L}}{\partial \dot{q}} - \frac{\partial \mathcal{L}}{\partial q} &= -R\dot{q}\end{aligned} \tag{27}$$

where the terms on the RHS of Eq. (27) are the generalized forces for $\eta(t)$ and $q(t)$. Removing the static term give the dynamic coupled electro-mechanical equations

$$\begin{aligned}&M_1\ddot{\eta} + M_Z\ddot{z} + D_1\dot{\eta} + K_L\eta + \alpha_1 q^2 + \alpha_2 q = 0 \\ &\dot{q} = -\frac{q}{\varepsilon_0 SR}\Big[\frac{T_{PDMS}}{\varepsilon_r} + d_0 - \phi(L_1)\eta\Big] + \frac{\sigma(d_0 - \phi(L_1)\eta)}{\varepsilon_0 R}\end{aligned} \tag{28}$$

where

$$
\begin{aligned}
M_1 &= m(x)\int_0^L \phi(x)^2 dx \\
M_Z &= m(x)\int_0^L \phi(x) dx \\
D_1 &= c\int_0^L \phi(x)^2 dx \\
K_L &= D(x)\int_0^L \phi''^2(x) dx - p\int_0^L \phi'^2(x) dx \\
\alpha_1 &= -\frac{\phi(L_1)}{2\varepsilon_0 S} \\
\alpha_2 &= \frac{\sigma\phi(L_1)}{\varepsilon_0} \\
\ddot{z} &= A_{amp}\cos\Omega t
\end{aligned}
\tag{29}
$$

By examining the parameters in Eq. (29), we see that as the compressive axial force is increased, the natural frequency will decrease due to the decreasing of the system's stiffness. The reduction of the stiffness in the system causes a softening effect on the system. Therefore increased axial forces will generate larger responses.

2.6 Impact Model

As there is an impact that occurs in this system, a separate equation of motion must be implemented for the case when the impact occurs. When the impact occurs, the upper electrode will penetrate into the PDMS layer, with the maximum penetration distance being δ such that $d_0 = g_i + \delta$. The impact forces and damping terms are shown with [13, 26]

$$
\begin{aligned}
F_i &= k_i\eta + (K_L - k_i)g_i \\
F_d &= c_i\dot{\eta}
\end{aligned}
\tag{30}
$$

Once Eq. (30) are substituted into Eq. (28), we arrive at full piecewise governing equations. Our governing equations for our complete system are shown below. The mechanical equation is represented as a piecewise function, with the condition being whether the upper electrode is in the air gap between itself and the PDMS layer or impacting the PDMS layer.

$$\begin{cases} M_1\ddot{\eta} + M_Z A_{amp}\cos\Omega t + D_1\dot{\eta} + K_L\eta + \alpha_1 q^2 + \alpha_2 q = 0 & y(L_1,t) < g_i \\ M_1\ddot{\eta} + M_Z A_{amp}\cos\Omega t + (D_1 + c_i)\dot{\eta} + (K_L + k_i)\eta - k_i g_i & \\ \qquad + \alpha_1 q^2 + \alpha_2 q = 0 & y(L_1,t) \geq g_i \end{cases}$$
$$\dot{q} = -\frac{q}{\varepsilon_0 SR}\Big[\frac{T_{PDMS}}{\varepsilon_r} + d_0 - \phi(L_1)\eta\Big] + \frac{\sigma(d_0 - \phi(L_1)\eta)}{\varepsilon_0 R} \tag{31}$$

2.7 Results and Discussions

Using the coupled reduced order equations, Eq. (31), we implement the Shooting Method to numerically solve for the frequency response of the system. The Shooting Method is a computationally efficient alternative to Long Time Integration as the response is iteratively calculated until the correct initial conditions are determined [27]. We now attempt to validate our model using previously performed experimental data as seen in [12], Fig. 4. We assume that the asymmetry of the added mass and upper electrode have no effect on the dynamics. We justify this because FEA simulations were performed for a asymmetric case and a symmetric case and the natural frequency did not change. Therefore the thickness of the center mass and upper electrode will be distributed such that we have symmetry.

Numerical parameters are defined in Table 2. Although the length of the beam from [12] is $10cm$, we used an effective length of $11cm$ to account for imperfect boundary conditions concerning the clamped edges in the mode shape analysis. Results show a close agreement between the model and the experiment. The deviations could be from estimation of the charge density or the electrical model

Table 2: Experimental parameters

Parameter	Value
$(L$ x b x $t)$	$(11$ x 3.7 x $0.1)cm$
$(L_m$ x b_m x $t_m)$	$(3.7$ x 5.2 x $0.45)cm$
c	$52\ {}^{Ns}/_{m}$
d_0	$260\ \mu m$
δ_1	$10\ \mu m$
g_i	$250\ \mu m$
E	$2.344\ GPa$
R	$2\ M\Omega$
T_{PDMS}	$500\ \mu m$
ε_r	2.5
ρ	$1220\ {}^{kg}/_{m^3}$
σ	variable
k_i	$2000\ {}^{N}/_{m}$
c_i	$5000\ {}^{Ns}/_{m}$

for the estimate for the charge. We believe developing an accurate electrical model requires further investigation.

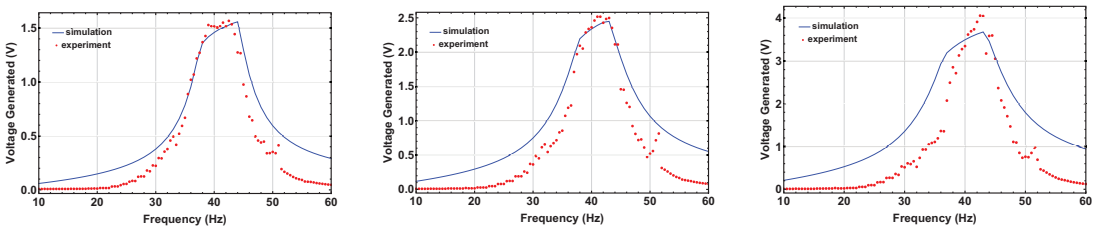

Figure 4: Experimental and simulated voltage frequency response curves using the continuous model: (a) $A_{amp} = 0.5g$, $\sigma = 3.2C/m^2$, (b) $A_{amp} = 0.6g$, $\sigma = 5.2C/m^2$, and (c) $A_{amp} = 0.7g$, $\sigma = 7.7C/m^2$

2.8 Free Vibration

As we have now determined that the continuous model is a viable model to predict the experimental data, we look at cases in which we include a compressive axial force in the system. The following sections include simulations of the system including the axial force to observe the characteristics of the system. Before we look at the impact dynamics with the axial force, we first explore the free vibration case

to gain insight to the systems response. Therefore we will be removing the amplitude limiter so there will be no impact and will be monitoring the displacement response. As the critical axial load is approximately $52N$, we will be limiting the axial force to be less than this value. We see in Fig. 5 that as we increase the axial force on the system, the natural frequency is shifted to the left and higher displacement responses are attained. This is consistent with our finding in Eq. (29) with the variable K_L. As the axial force increases, the parameter K_L decreases, which effectively softens the system. This softening behavior allows the system to respond at higher amplitudes than the no axial force case. The addition of the axial force is very useful because the system can be tuned to various natural frequencies and higher voltage responses can be attained. As the free vibration displacement responses are larger, we expect the maximum velocity to increase as well. And since we have an amplitude limiter (lower electrode), the axial force will allow for a harder impact due to the increased velocity for cases with the same gap. In addition to the higher voltage amplitudes, we expect a larger operating bandwidth. Again this is attributed to the amplitude limiter in the system, which will allow the electrodes to contact each other over a broader frequency range.

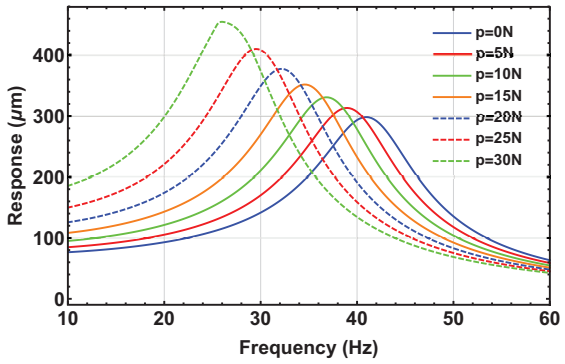

Figure 5: Free vibration of the system with no impact.

2.9 Numerical Simulations

Now that we have gained insight concerning the response of the system with the addition of a compressive axial force, we perform simulations to show what the characteristic response curves of the system could be under different axial forces,

initial gaps, and load resistances. The acceleration amplitude that was used for this numerical section is $A_{amp} = 0.5g$, see Figs. 6 to 8. In Figs. 6 to 8, the surface charge density is increased with larger axial forces. This is consistent with increasing the surface charge density with higher acceleration amplitudes because in both of these cases, whether we have an axial force or a higher acceleration amplitude, we have a harder impact and a larger penetration [12].

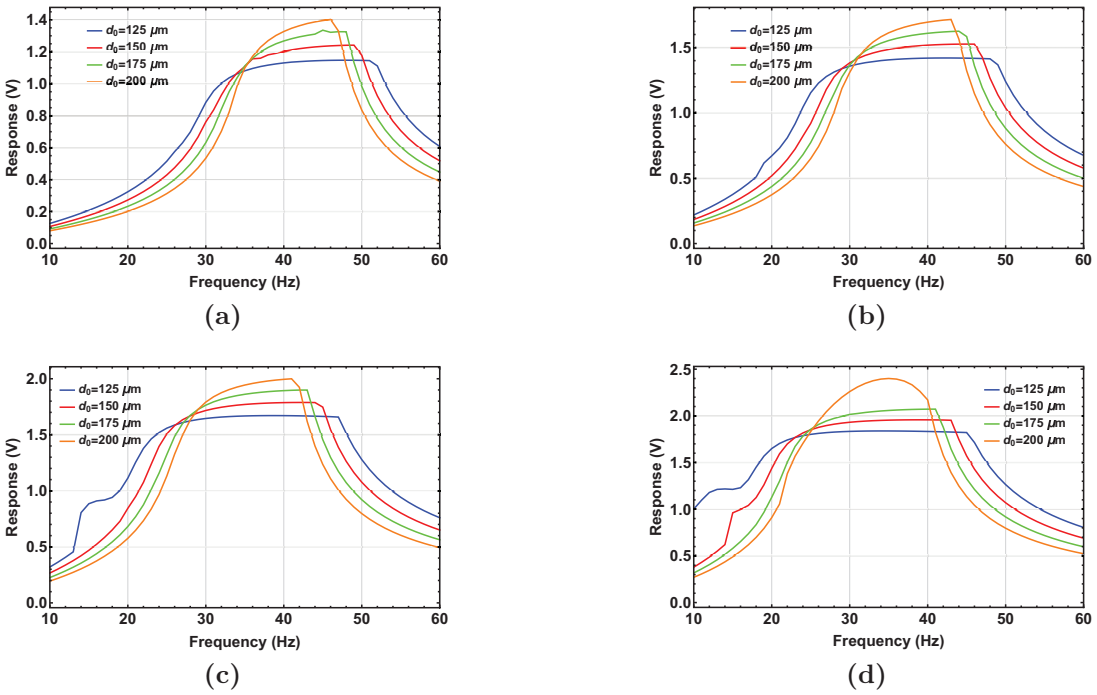

Figure 6: Simulated voltage frequency response curves for an excitation amplitude of $0.5g$, a variable gap, and: (a) $p = 0N$, (b) $p = 10N$, (c) $p = 15N$, (d) $p = 20N$

Fig. 6 illustrates that regardless of the value of the axial force, the bandwidth increases as the initial gap decreases as expected. With smaller initial gaps, wider frequency bandwidths are obtained.

Keeping the gap constant and increasing the axial force widens the frequency bandwidth, see Fig. 7. We also see that with the increased axial force, we have a larger voltage output regardless of the gap. Results indicate that as the axial force increase, the impact on the harvester and thus more charge and voltage are generated because of the larger penetration in the PDMS layer. From Figs. 6 and 7, we realize that depending on the application, the system can be tuned to accommodate the frequency range of interest. Some applications might require a

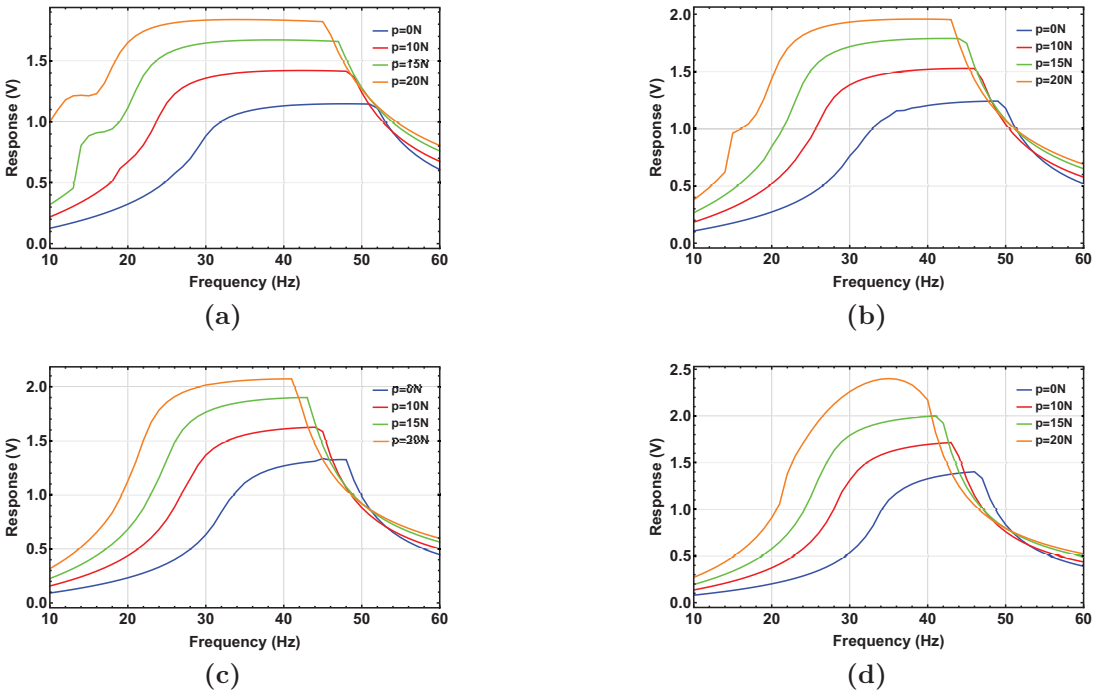

Figure 7: Simulated voltage frequency response curves for an excitation amplitude of $0.5g$, a variable axial force, and: (a) $d_0 = 125\mu m$, (b) $d_0 = 150\mu m$, (c) $d_0 = 175\mu m$, (d) $d_0 = 200\mu m$

larger bandwidth even with the smaller voltage amplitudes, or higher amplitudes with smaller bandwidths might be desired. And of course, the ability to tune the frequency to different values is advantageous in applications where the system can dynamically change.

As the power output of an energy harvester is one of the characteristics that determine its effectiveness, we will briefly explore how varying the load resistance changes the power output. Derived from Ohm's Law, we know that $P = \frac{V^2}{R}$, where $V = IR$. We notice that there will be a limit at which increasing the load resistance will not increase the power output any further as the current depends on the resistance as well. We seek to determine the optimal load resistance for the system, and to determine whether or not the compressive axial force will impact the optimal load resistance. We consider cases where we have $p = 0N$ and $p = 10N$. With the addition of the axial force, we see that the optimal resistance of the system is approximately $60M\Omega$ and $70M\Omega$ for $p = 0N$ and $p = 10N$ respectively. Therefore, we see that the optimal load resistance of the system is dependent on the compressive axial force and that it does not remain constant.

That means if the axial force is changed to accommodate the frequency range of interest, the load resistance must be changed accordingly because of the coupling nature of the electro-mechanical system. The presented model described the interactions of mechanical and electrical components and can be used as an effective design tool for high performance triboelectric energy harvesters with tunable wide bandwidths.

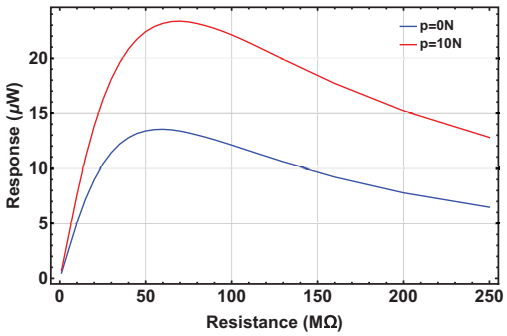

Figure 8: Determining maximum power output for an excitation amplitude of $0.5g$, initial gap of $200\mu m$, and different axial forces

2.10 Experimental Setup and Results

To experimentally test the concept of the wideband energy harvester, the system was placed on an electrodynamic shaker. A figure of the experimental setup is shown in Fig. 9. The input signal to the shaker was controlled in a closed loop with Matlab. The signal was sent to a data acquisition device (NI USB-6251), then though a power amplifier (Techron 5530 Power Supply Amplifier), and then to the shaker. An accelerometer (PCB Piezotronics 352A24) was placed on the base of the shaker and the accelerometer signal was used in the feedback control loop. The accelerometer signal was sent through an amplifier (Kistler Dual Mode Amplifier) and was then sent to the DAQ. The voltage was recorded using an oscilloscope (Tektronix MDO3034). The axial force was controlled by adjusting a screw that was fixed to the setup, and the axial force was measured using a FlexiForce Sensor. The power amplifier that powers the electrodynamic shaker is not pictured.

Using different parameters than the simulation, we explored some preliminary

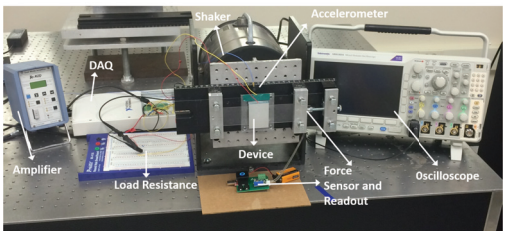

Figure 9: Picture of the experimental setup

experimental trials. We included multiple axial force cases with various excitation amplitudes. As we from Figs. 10 and 11, as the axial force is increased, the natural frequency decreases and higher voltage responses are attained. Larger bandwidths are also obtained. In the region where the impact occurs, we see a dramatic increase in the voltage response, which we did not observe in the model. The experimental results look promising, and the fit to the simulations has the same characteristic shape.

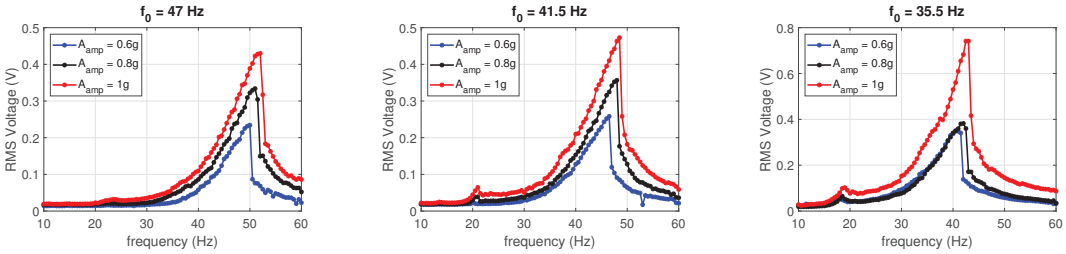

Figure 10: Frequency response curves for various excitation amplitudes and natural frequencies

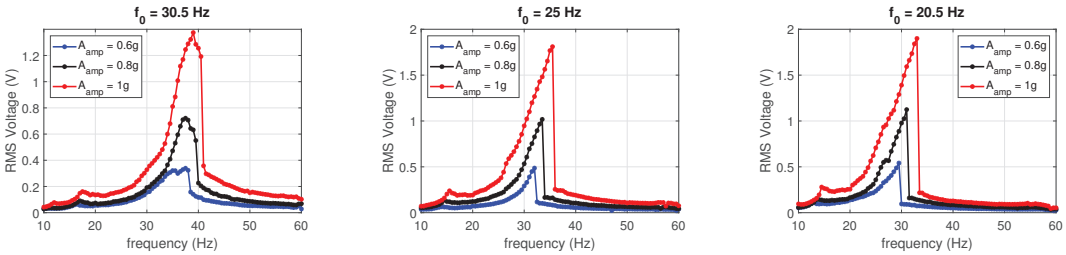

Figure 11: Frequency response curves for various excitation amplitudes and natural frequencies

2.11 Conclusions

A design for a tunable wideband energy harvester using triboelectric transduction was proposed. This research intends to take advantage of impact vibration that naturally occurs in triboelectric generators and combine it with the effect of a compressive force to make a tunable energy harvester. A full continuous model was derived using linear Euler-Bernoulli beam theory. The modeling of the beam accounted for the large paddle-like mass located at the midspan, reflected in the mode shape. The continuous coupled electromechanical model was then validated partially with previously obtained experimental data [12]. The addition of the axial force softened the system, which would allow the system to attain greater free vibration displacement amplitudes. Because of the stopper, the addition of the axial force will result in harder impacts and higher voltage response amplitudes. We saw that for a constant initial electrode gap, the addition of the increased axial force lowered the frequency range and generated a larger operating bandwidth. Keeping the axial force constant and decreasing the gap results in larger bandwidths at lower amplitudes. The optimal load resistance where the peak power can be extracted was found to be a function of the axial load. In summary, with the increased axial force, we were able to see higher voltage responses over larger operating bandwidths. The axial force also allowed the system to be tuned to a wide range of natural frequencies to accommodate different frequency sources. Due to the addition of the triboelectric transduction mechanism, the system has the potential to be self-powered, which is advantageous for the powering of wireless batteries and sensors for health monitoring applications.

3 Bi-stable Triboelectric Shock Sensor

3.1 Introduction

Shock sensors have a wide application in the auto-industry [28], recycle systems in aerospace [29], fuse systems [30], earthquake detection [31] airbag systems [32–34], weapons arming and disarming [35, 36], and senior fall detection [37]. Fast response, high sensitivity, and reliability are considered major requirements for shock sensors. Different actuation mechanisms have been investigated: mechanical [38, 39], electrostatic [40–43], electrothermal [44–46], piezoelectric [47–52], optical actuation [53] and electromagnetic [54, 55]. Among all previous mechanisms, electrostatic actuators are the most common. However, they often require a voltage multiplier because of the large operating voltages. Electromagnetic actuators continually consume large amounts of power (in the mW range). To avoid the requirement of continuous powering, mechanical buckling offers two stable, switchable states [45, 56]. The simplest mechanical structures for buckling are bi-stable buckled beams or shallow arches that can achieve high displacements at low actuation. They are ideal for systems that require on and off or open and closed positions because of their high speed and tunability. Harmonic excitation can switch the beam between the two stable positions [57, 58] . A critical amount of energy introduced to the actuator activates the transition of the system between those stable points [59, 60].

Many studies have been conducted on threshold acceleration sensors, which are also referred to as g-sensors in the literature. The concept of a threshold sensor is that the sensor will switch stable states when the acceleration level exceeds a threshold value and will remain stationary while the acceleration level is below the threshold. Acceleration sensors can be designed based on cantilever beams [61–63], clamped-clamped beams [29], and other features [33, 64].

When sufficient force is applied, the structure moves from one stable point to another by snap-through motion. This snap-through motion will usually open or close a circuit or send a signal using a transducer to indicate that the device has switched states. Triboelectric transducers are emerging as a conversion mechanism because of their great energy density and easy, low-cost fabrication [12, 65]. Their requirement of contact and separation makes them useful for shock (impact) sensing. Many current designs cannot distinguish when the shock gets past a limit. Building triboelectric transducers with a bi-stable structure enables making threshold sensors that activate beyond a shock limit and provide more information about the magnitude of the shock.

This work will demonstrate the feasibility of a threshold sensor that uses triboelectric transduction. It uses the bi-stable mechanism of a buckled clamped-clamped beam with an aluminum layer, a triboelectric material, attached at the center of the beam. Initially, a static axial compressive load buckles the straight beam to its stable, upper position. When the excitation acceleration exceeds a threshold, the buckled beam will snap to its lower stable position, and the aluminum layer strikes the lower PDMS layer, another triboelectric material as seen in Fig. 12. During this transition, there will be a rapid change in potential energy of the structure that is converted to a voltage spike in the triboelectric transducer. The threshold shock can be tuned using the initial compressive load. In addition, because the voltage spike is a function of the impact, the threshold sensor acts as an accelerometer beyond the threshold shock. The result is a tunable triboelectric threshold sensor with greater performance and enhanced functionality than existing sensors. To accurately simulate the sensor behavior, a continuous electro-mechanical model based on the nonlinear Euler-Bernoulli beam theory was developed to capture the dynamical responses. This effort on the macro-prototype of the shock sensor provides a fundamental understanding of the electro-mechanical system response and a design platform for its future miniature development.

The organization of this chapter is as follows. The principle of operation of the

sensor will be described. Then a continuous model will be introduced, deriving the static configuration, mode shape, and reduced order model. The impact model will be described and the experimental setup will be displayed in detail. Comparisons between theoretical and experimental trials will be shown to prove the validity of the model. The discussion ends with a conclusion.

3.2 Nomenclature

Table 3: Nomenclature for Chapter 3

Parameter	Description
A	Cross-sectional area of beam
b, b_m	Width of beam, width of center mass and upper electrode
B	Arbitrary constant
c, c_i	Damping term, impact damping term
d_0	Initial total gap with no compressive axial load
D_1	Damping coefficient
E	Young's Modulus
E_{air}, E_{PDMS}	Electric field in air gap, PDMS layer
F_d, F_s	Impact damping force, impact stiffness force
g_i	Initial gap between upper electrode and PDMS
I	Moment of inertia
J	Jacobian
K_L, K_Q, K_C, k_i	Linear, quadratic, cubic, impact stiffness coefficients
L, L_m	Length of beam, length of center mass and upper electrode
L_1	Midspan location and location of concentrated mass
M	Concentrated mass consisting of center mass and upper electrode
M_1, M_z	Mass coefficient, base excitation mass coefficient
p	Compressive axial force
$q(t)$	Charge transferred

Continued on next page

Table 3 – *Continued from previous page*

Parameter	**Description**
R	Load resistance
s	Constant for mode shape analysis
S	Contact area
t, t_m	Thickness of beam, thickness of center mass and upper electrode
T	Kinetic Energy
T_{PMDS}	Thickness of PDMS layer
$u(x,t)$	Longitudinal deflection of the beam
U	Potential Energy
$v(x,t)$	Dynamic deflection about buckled configuration
V	Volume
$w(x,t)$	Absolute transverse deflection of the beam
W_{nc}	Work done by the nonconservative forces
$y(x,t)$	Relative transverse deflection of the beam
$z(t)$	Base excitation
z_c	Transverse coordinate direction
α, β	Constants for mode shape analysis
$\alpha_{1,2,3}$	Electrical constants
$\gamma_i(t)$	Time dependent function
δ_1	Penetration distance
$\varepsilon, \varepsilon_0, \varepsilon_r$	Permittivity, vacuum permittivity, relative permittivity
ε_s	Mechanical strain
$\eta(t)$	Arbitrary time dependent function
λ, λ_1	Eigenvalues
ρ	Density of polymer beam
σ	Surface charge density
σ_s	Mechanical stress
$\phi(x)$	Mode shape
$\psi(x)$	Buckled/Static configuration
ω	Natural frequency

3.3 Principle of Operation

The principle of operation of the shock sensor is shown in Figs. 12a and 12b. The figures show the upper and lower stable configurations of the threshold sensor. We increase the axial force on an initially straight beam until the buckling phenomenon occurs (Fig. 12). In the initial configuration, when the upper and lower electrodes are separated, there is a charge equilibrium, so there is no voltage across the load. Once the device is triggered, the upper electrode travels towards the lower electrode and as the gap changes, the electrical potential difference also changes. Two factors that affect the voltage potential difference are added mass at the midspan of the beam and the velocity of the upper electrode. With a larger center mass, the inertial force will be greater that will result in a higher velocity of the upper electrode. With this higher velocity, there will be a larger change in potential difference. Once the upper and lower electrodes come in contact with each other, the voltage potential difference quickly drops to zero. The voltage potential will remain at zero while the device remains at the lower configuration. Next, the mathematical model of the coupled electro-mechanical system will be developed to shed light on the system behavior.

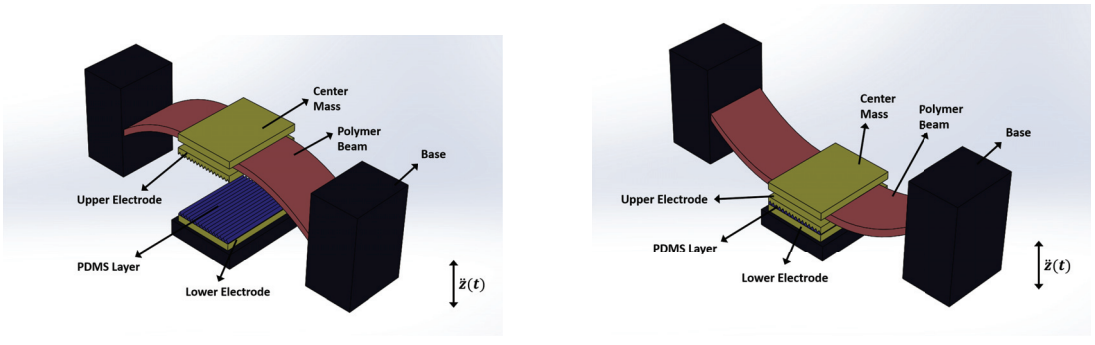

(a) (b)

Figure 12: The working principle of the threshold shock sensor when the base experiences a shock input: (a) the initial buckled position held stable by the axial load; (b) the triggered position when the force from a shock exceeds a threshold and switches stable positions. The figure is not to scale.

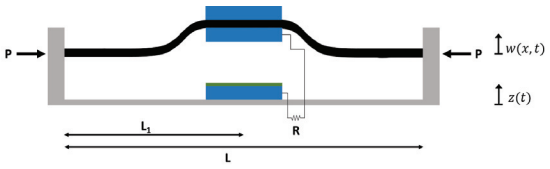

Figure 13: Schematic of shock sensor. Some features are exaggerated to help the reader visualize the system.

3.4 Mathematical Modeling

Because this system includes large deformations of the beam, a large mass located at the center of the beam, and an axial force, we will develop a continuous model to accurately describe its behavior, Fig. 13. The continuous model is chosen because: (i) it is more accurate than a lumped parameter model; (ii) the effect of the mid-plane stretching will not have to be determined experimentally; and (iii) the axial force can be easily incorporated into the model. To reduce the complexity of the continuous system, we will assume that the added center mass and the upper aluminum layer at the midpoint is a concentrated mass. Because buckling occurs, we include the effect of the mid-plane stretching that introduces a geometric nonlinearity into the system. To develop our equations of motion we first describe our system. Because we are considering our system to be a beam with a concentrated mass located at the midspan, our model will split the beam into two spans.

We note that although the transverse direction is in the same direction as the gravitational force, we will neglect the effect of the gravitational force in the model because the static configurations of the system are dominated by the buckling phenomenon and not by gravity. The one parameter that would be changed by including the effect of gravity in the model is the threshold acceleration. As this study is only a proof of concept and a learning tool for the dynamics and physics of the system, we are only concerned with whether a switching event occurs. Finding the exact threshold acceleration is not the driving factor for this study. At this point, we are only concerned with demonstrating the feasibility of a triboelectric threshold shock sensor.

3.4.1 Deriving Equations of Motion

The equations of motion of this system will be derived using the Extended Hamilton's Principle and we start by representing the system in terms of the absolute deflection of the beam and the base motion. If we assume the longitudinal inertia to be negligible, the kinetic energy of the system can be written as

$$T = \frac{1}{2}\rho A \int_0^{L_1} \dot{w}_1^2 dx + \frac{1}{2}\rho A \int_{L_1}^{L} \dot{w}_2^2 dx + \frac{1}{2} M \dot{w}_1^2(L_1) \tag{32}$$

The potential energy is expressed as

$$U = \frac{1}{2}\int_V \varepsilon_s \sigma_s dV + \frac{\varepsilon_0}{2}\int_V E_{air}^2 dV + \frac{\varepsilon_0 \varepsilon_r}{2}\int_V E_{PDMS}^2 dV \tag{33}$$

where

$$\begin{aligned} \varepsilon_s &= u_i' + \frac{1}{2} w_i'^2 - z_c w_i'' \\ \sigma_s &= E\varepsilon_s \\ E_{air} &= \frac{(-q + \sigma S)}{\varepsilon_0 S} \\ E_{PDMS} &= -\frac{q}{\varepsilon_0 \varepsilon_r S} \end{aligned} \tag{34}$$

Expanding Eq. (33) we get

$$
\begin{aligned}
U = & \frac{1}{2}E\int_{-b/2}^{b/2}dy_c\int_{-h/2}^{h/2}dz_c\int_0^{L_1}(u_1'+\frac{1}{2}w_1'^2)^2dx+\frac{1}{2}E\int_{-b/2}^{b/2}dy_c\int_{-h/2}^{h/2}z_c^2dz_c\int_0^{L_1}w_1''^2dx \\
& -E\int_{-b/2}^{b/2}dy_c\int_{-h/2}^{h/2}z_cdz_c\int_0^{L_1}(u_1'+\frac{1}{2}w_1'^2)w_1''dx \\
& +\frac{1}{2}E\int_{-b/2}^{b/2}dy_c\int_{-h/2}^{h/2}dz_c\int_{L_1}^{L}(u_2'+\frac{1}{2}w_2'^2)^2dx+\frac{1}{2}E\int_{-b/2}^{b/2}dy_c\int_{-h/2}^{h/2}z_c^2dz_c\int_{L_1}^{L}w_2''^2dx \\
& -E\int_{-b/2}^{b/2}dy_c\int_{-h/2}^{h/2}z_cdz_c\int_{L_1}^{L}(u_2'+\frac{1}{2}w_2'^2)w_2''dx \\
& +\frac{\varepsilon_0\varepsilon_r}{2}\int_{-b_m/2}^{b_m/2}dy_c\int_{L_1-L_m/2}^{L_1+L_m/2}dx\int_{-d_0}^{-d_0+T_{PDMS}}\frac{q^2}{\varepsilon_0^2\varepsilon_r^2S^2}dz_c \\
& +\frac{\varepsilon_0}{2}\int_{-b_m/2}^{b_m/2}dy_c\int_{L_1-L_m/2}^{L_1+L_m/2}dx\int_{-d_0}^{w_1(L_1)-z(t)}\Big(\frac{q^2}{\varepsilon_0^2S^2}+\frac{\sigma^2}{\varepsilon_0^2}-\frac{2q\sigma}{\varepsilon_0^2S}\Big)dz_c
\end{aligned}
\tag{35}
$$

We simplify Eq. (35) are represent the potential energy as

$$
\begin{aligned}
U = & \frac{1}{2}EI\int_0^{L_1}w_1''^2dx+\frac{1}{2}EI\int_{L_1}^{L}w_2''^2dx+\frac{EA}{2}\int_0^{L_1}\Big(u_1'+\frac{1}{2}w_1'^2\Big)^2dx \\
& +\frac{EA}{2}\int_{L_1}^{L}\Big(u_2'+\frac{1}{2}w_2'^2\Big)^2dx+\frac{T_{PDMS}}{2\varepsilon_0\varepsilon_rS}q^2+\frac{d_0+w_1(L_1)-z(t)}{2\varepsilon_0S}q^2 \\
& -\frac{\sigma(d_0+w_1(L_1)-z(t))}{\varepsilon_0}q+\frac{\sigma^2S(d_0+w_1(L_1)-z(t))}{2\varepsilon_0}
\end{aligned}
\tag{36}
$$

The variation of the work due to the nonconservative forces is

$$
\delta W_{nc} = -c\int_0^{L_1}\dot{w}_1\delta w_1dx-c\int_{L_1}^{L}\dot{w}_2\delta w_2dx-R\dot{q}\delta q+pu_1(0)-pu_2(L) \tag{37}
$$

Now that the system has been fully represented in terms of the absolute deflection, we now represent Eqs. (32), (36) and (37) in terms of the relative motion, $y_i(x,t)$, such that: $w_i(x,t) = y_i(x,t) + z(t)$. The variation of the kinetic and potential energies are now derived.

$$\delta T = \rho A \int_0^{L_1} (\dot{y}_1 + \dot{z})\delta\dot{y}_1 dx + \rho A \int_{L_1}^{L} (\dot{y}_2 + \dot{z})\delta\dot{y}_2 dx + M(\dot{y}_1^2(L_1) + z(t))\delta\dot{y}_1(L_1) \tag{38}$$

$$\begin{aligned}\delta U =& EI \int_0^{L_1} y_1'' \delta y_1'' dx + EI \int_{L_1}^{L} y_2'' \delta y_2'' dx + EA \int_0^{L_1} \Big(u_1' + \frac{1}{2}y_1'^2\Big)(\delta u_1' + y_1'\delta y_1')dx \\ &+ EA \int_{L_1}^{L} \Big(u_2' + \frac{1}{2}y_2'^2\Big)(\delta u_2' + y_2'\delta y_2')dx + \frac{T_{PDMS}}{\varepsilon_0\varepsilon_r S} q\delta q + \frac{d_0 + y_1(L_1)}{\varepsilon_0 S} q\delta q \\ &+ \frac{q^2}{2\varepsilon_0 S}\delta y_1(L_1) - \frac{\sigma\Big(d_0 + y_1(L_1)\Big)}{\varepsilon_0}\delta q - \frac{\sigma q}{\varepsilon_0}\delta y_1(L_1) + \frac{\sigma^2 S}{2\varepsilon_0}\delta y_1(L_1)\end{aligned} \tag{39}$$

The Extended Hamilton's Principle, $\int_{t_1}^{t_2}(\delta T - \delta U + \delta W_{nc})dt = 0$ is now performed. We break the Extended Hamilton's Principle into three parts.

$$\begin{aligned}\int_{t_1}^{t_2} \delta T dt =& \int_0^{L_1} \Big[\rho A(\dot{y}_1 + \dot{z})\delta y_1\Big|_{t_1}^{t_2} - \int_{t_1}^{t_2} \rho A(\ddot{y}_1 + \ddot{z})\delta y_1 dt\Big] dx \\ &+ \int_{L_1}^{L} \Big[\rho A(\dot{y}_2 + \dot{z})\delta y_2\Big|_{t_1}^{t_2} - \int_{t_1}^{t_2} \rho A(\ddot{y}_2 + \ddot{z})\delta y_2 dt\Big] dx \\ &+ M(\dot{y}_1(L_1) + \dot{z})\delta y_1(L_1)\Big|_{t_1}^{t_2} - \int_{t_1}^{t_2} M(\ddot{y}_1(L_1) + \ddot{z})\delta y_1(L_1) dt\end{aligned} \tag{40}$$

Using the definition of virtual work, we simplify Eq. (40)

$$\begin{aligned}\int_{t_1}^{t_2} \delta T dt = \int_{t_1}^{t_2} \Bigg[&- \int_0^{L_1} \rho A(\ddot{y}_1 + \ddot{z})\delta y_1 dx - \int_{L_1}^{L} \rho A(\ddot{y}_2 + \ddot{z})\delta y_2 dx \\ &- M(\ddot{y}_1(L_1) + \ddot{z})\delta y_1(L_1)\Bigg] dt\end{aligned} \tag{41}$$

We now consider Hamilton's Principle for the potential energy.

$$
\begin{aligned}
\int_{t_1}^{t_2} \delta U dt = \int_{t_1}^{t_2} \Bigg[& EIy_1'' \delta y_1' \Big|_0^{L_1} - EIy_1''' \delta y_1 \Big|_0^{L_1} + EI \int_0^{L_1} y_1'''' \delta y_1 dx \\
& + EIy_2'' \delta y_2' \Big|_{L_1}^{L} - EIy_2''' \delta y_2 \Big|_{L_1}^{L} + EI \int_{L_1}^{L} y_2'''' \delta y_2 dx \\
& + EA\Big(u_1' + \frac{1}{2}y_1'^2\Big)\delta u_1 \Big|_0^{L_1} - EA \int_0^{L_1} \Big(u_1' + \frac{1}{2}y_1'^2\Big)' \delta u_1 dx \\
& + EA\Big(u_1' + \frac{1}{2}y_1'^2\Big)y_1' \delta y_1 \Big|_0^{L_1} - EA \int_0^{L_1} \Big[\Big(u_1' + \frac{1}{2}y_1'^2\Big)y_1'\Big]' \delta y_1 dx \\
& + EA\Big(u_2' + \frac{1}{2}y_2'^2\Big)\delta u_2 \Big|_{L_1}^{L} - EA \int_{L_1}^{L} \Big(u_2' + \frac{1}{2}y_2'^2\Big)' \delta u_2 dx \\
& + EA\Big(u_2' + \frac{1}{2}y_2'^2\Big)y_2' \delta y_2 \Big|_{L_1}^{L} - EA \int_{L_1}^{L} \Big[\Big(u_2' + \frac{1}{2}y_2'^2\Big)y_2'\Big]' \delta y_2 dx \\
& + \frac{T_{PDMS}}{\varepsilon_0 \varepsilon_r S} q \delta q + \frac{d_0 + y_1(L_1)}{\varepsilon_0 S} q \delta q + \frac{q^2}{2\varepsilon_0 S} \delta y_1(L_1) \\
& - \frac{\sigma\Big(d_0 + y_1(L_1)\Big)}{\varepsilon_0} \delta q - \frac{\sigma q}{\varepsilon_0} \delta y_1(L_1) + \frac{\sigma^2 S}{2\varepsilon_0} \delta y_1(L_1) \Bigg] dt
\end{aligned}
\tag{42}
$$

Performing Hamilton's Principle on the work due to nonconservative forces,

$$
\int_{t_1}^{t_2} \delta W_{nc} dt = \int_{t_1}^{t_2} \Bigg[- c \int_0^{L_1} \dot{y}_1 \delta y_1 dx - c \int_{L_1}^{L} \dot{y}_2 \delta y_2 dx - R\dot{q}\delta q + pu_1(0) - pu_2(L) \Bigg] dt \tag{43}
$$

By now considering all of the terms of the Extended Hamilton's Principle, we obtain the governing equations for the transverse motion, the longitudinal motion, and the charge.

$$
\begin{cases}
\rho A\ddot{y}_1 + \rho A\ddot{z} + c\dot{y}_1 + EIy_1'''' - EA\Big[(u_1' + \frac{1}{2}y_1'^2)y_1'\Big]' = 0 \quad 0 \le x \le L_1 \\
\rho A\ddot{y}_2 + \rho A\ddot{z} + c\dot{y}_2 + EIy_2'''' - EA\Big[(u_2' + \frac{1}{2}y_2'^2)y_2'\Big]' = 0 \quad L_1 \le x \le L
\end{cases}
$$

$$
\begin{cases}
EA\Big[u_1' + \frac{1}{2}y_1'^2\Big]' = 0 \quad 0 \le x \le L_1 \\
EA\Big[u_2' + \frac{1}{2}y_2'^2\Big]' = 0 \quad L_1 \le x \le L
\end{cases}
\tag{44}
$$

$$
\dot{q} = \frac{-q}{\varepsilon_0 RS}\Big[\frac{T_{PDMS}}{\varepsilon_r} + d_0 + y_1(L_1)\Big] + \frac{\sigma(d_0 + y_1(L_1))}{\varepsilon_0 R}
$$

To decouple the transverse and longitudinal equations of motion, we first consider the longitudinal equations of motion. Using Eq. (44) and neglecting the longitudinal inertia, we develop the governing equations for the longitudinal direction, as well as the boundary conditions from the Extended Hamilton's Principle and simple axial displacement calculations.

$$
\begin{cases}
u_1(x) = \gamma_1(t)x + \gamma_2(t) - \int_0^x \frac{1}{2}y_1'^2 dx \\
u_2(x) = \gamma_3(t)(x - L_1) + \gamma_4(t) - \int_{L_1}^x \frac{1}{2}y_2'^2 dx \\
u_1(0) = \frac{pL_1}{EA} \\
u_2(L) = -\frac{p(L-L_1)}{EA} \\
u_1(L_1) = u_2(L_1) \\
EA\Big[u_1'(L_1) + \frac{1}{2}y_1'^2(L_1)\Big] = EA\Big[u_2'(L_1) + \frac{1}{2}y_2'^2(L_1)\Big]
\end{cases}
\tag{45}
$$

From the third part of Eq. (45) we have

$$
u_1(0) = \gamma 2(t) = \frac{pL_1}{EA} \tag{46}
$$

From the fourth part of Eq. (45) we have

$$u_2(L) = \gamma_3(t)(L - L_1) + \gamma_4(t) - \int_{L_1}^{L} \frac{1}{2} y_2'^2 \, dx = -\frac{p(L - L_1)}{EA} \tag{47}$$

Using the continuity equation at $x = L_1$ and Eqs. (46) and (47), we have

$$\begin{aligned} u_1(L_1) = u_2(L_1) = \gamma_1(t)L_1 + \frac{pL_1}{EA} - \int_0^{L_1} \frac{1}{2} y_1'^2 \, dx = -\frac{p(L - L_1)}{EA} - \gamma_3(t)(L - L_1) \\ + \int_{L_1}^{L} \frac{1}{2} y_2'^2 \, dx \end{aligned} \tag{48}$$

To further simplify, we note that while expanding the governing equations for the longitudinal direction, we determined that

$$\begin{aligned} u_1'(x) + \frac{1}{2} y_1'^2(x) = \gamma_1(t) \\ u_2'(x) + \frac{1}{2} y_2'^2(x) = \gamma_3(t) \end{aligned} \tag{49}$$

From the last part of Eq. (45) we see that at $x = L_1$, that $u_1'(L_1) + \frac{1}{2} y_1'^2(L_1) = u_2'(L_1) + \frac{1}{2} y_2'^2(L_1)$. Using this information along with Eq. (49), we conclude that $\gamma_1(t) = \gamma_3(t)$. Now simplifying Eq. (48), we conclude that

$$\gamma_1(t) = \gamma_3(t) = -\frac{p}{EA} + \frac{1}{2L} \int_0^{L_1} y_1'^2 \, dx + \frac{1}{2L} \int_{L_1}^{L} y_2'^2 \, dx \tag{50}$$

Substituting Eq. (50) into the transverse equation of motion in Eq. (44), we get

$$
\begin{cases}
\begin{cases}
\rho A\ddot{y}_1 + \rho A\ddot{z} + c\dot{y}_1 + EIy_1'''' + py_1'' - \frac{EA}{2L}y_1''\left[\int_0^{L_1} y_1'^2 dx + \int_{L_1}^{L} y_2'^2 dx\right] = 0 \quad 0 \le x \le L_1 \\
\rho A\ddot{y}_2 + \rho A\ddot{z} + c\dot{y}_2 + EIy_2'''' + py_2'' - \frac{EA}{2L}y_2''\left[\int_0^{L_1} y_1'^2 dx + \int_{L_1}^{L} y_2'^2 dx\right] = 0 \quad L_1 \le x \le L
\end{cases} \\
\dot{q} = \frac{-q}{\varepsilon_0 RS}\left[\frac{T_{PDMS}}{\varepsilon_r} + d_0 + y_1(L_1)\right] + \frac{\sigma(d_0 + y_1(L_1))}{\varepsilon_0 R} \\
y_1(0) = 0 \\
y_2(L) = 0 \\
y_1'(0) = 0 \\
y_2'(L) = 0 \\
y_1(L_1) = y_2(L_1) \\
y_1'(L_1) = y_2'(L_1) \\
y_1''(L_1) = y_2''(L_1) \\
-M\ddot{y}_1(L_1) + EIy_1''' - EIy_2''' + \frac{q^2}{2\varepsilon_0 S} + \frac{\sigma^2 S}{2\varepsilon_0} - \frac{\sigma q}{\varepsilon_0} = 0
\end{cases}
\tag{51}
$$

3.4.2 Static Buckled Configuration

To determine the static solution of the system, we set the time dependent variables in Eq. (51) to zero. We neglect all electrical terms because the static configuration is dependent only on the mechanical system. We note that the static configuration of the system will be the trivial solution unless the compressive axial load is greater than the first critical axial load. In determining the static configuration and the mode shapes, we will be following similar procedures from [66]. Letting the static solution be $y_i(x,t) = \psi_i(x)$ results in the static equilibrium equation and boundary conditions of

$$\begin{cases} EI\psi_1'''' + p\psi_1'' - \frac{EA}{2L}\psi_1''\Big[\int_0^{L_1}\psi_1'^2 dx + \int_{L_1}^{L}\psi_2'^2 dx\Big] = 0 \quad 0 \le x \le L_1 \\ \\ EI\psi_2'''' + p\psi_2'' - \frac{EA}{2L}\psi_2''\Big[\int_0^{L_1}\psi_1'^2 dx + \int_{L_1}^{L}\psi_2'^2 dx\Big] = 0 \quad L_1 \le x \le L \end{cases} \tag{52}$$

$$\begin{cases} \psi_1(0) = 0 \\ \psi_1'(0) = 0 \\ \psi_2(L) = 0 \\ \psi_2'(L) = 0 \\ \psi_1(L_1) = \psi_2(L_1) \\ \psi_1'(L_1) = \psi_2'(L_1) \\ \psi_1''(L_1) = \psi_2''(L_1) \\ \psi_1'''(L_1) = \psi_2'''(L_1) \end{cases} \tag{53}$$

This is an eigenvalue problem with eigenvalues

$$\lambda^2 = \frac{p}{EI} - \frac{A}{2IL}\Big[\int_0^{L_1}\psi_1'^2 dx + \int_{L_1}^{L}\psi_2'^2 dx\Big] \tag{54}$$

Therefore, the solution takes the form of

$$\begin{aligned} \psi_1(x) &= B_1 + B_2 x + B_3\cos\lambda x + B_4\sin\lambda x \\ \psi_2(x) &= B_5 + B_6 x + B_7\cos\lambda x + B_8\sin\lambda x \end{aligned} \tag{55}$$

By using Eq. (55) with the associated boundary conditions, a coefficient matrix is found. The first eigenvalue is obtained by equating the determinant of the

coefficient matrix to zero. As we have nine unknowns and eight of them have been determined by using all but one of the boundary conditions, we still have one unknown constant. After an axial force (that is beyond the critical axial load) has been chosen, we use the last constraint, Eq. (54) to determine the last unknown constant to fully determine the static buckled configuration.

3.4.3 Determine Mode Shapes

The mode shapes and natural frequencies of the system around the buckled configuration are determined next. Because we are concerned with the vibrations around the buckled configuration, we let

$$y_i(x,t) = \psi_i(x) + v_i(x,t) \tag{56}$$

Eq. (56) is then substituted into the beam equations of motion in Eq. (51) and the forcing and damping terms are neglected.

$$\begin{cases} \rho A\ddot{v}_1 + EI\psi_1'''' + EIv_1'''' + p\psi_1'' + pv_1'' - \frac{EA}{2L}\psi_1''\Big[\int_0^{L_1}(\psi_1'+v_1')^2dx \\ \qquad + \int_{L_1}^{L}(\psi_2'+v_2')^2dx\Big] - \frac{EA}{2L}v_1''\Big[\int_0^{L_1}(\psi_1'+v_1')^2dx + \int_{L_1}^{L}(\psi_2'+v_2')^2dx\Big] = 0 \quad 0 \le x \le L_1 \\ \\ \rho A\ddot{v}_2 + EI\psi_2'''' + EIv_2'''' + p\psi_2'' + pv_2'' - \frac{EA}{2L}\psi_2''\Big[\int_0^{L_1}(\psi_1'+v_1')^2dx \\ \qquad + \int_{L_1}^{L}(\psi_2'+v_2')^2dx\Big] - \frac{EA}{2L}v_2''\Big[\int_0^{L_1}(\psi_1'+v_1')^2dx + \int_{L_1}^{L}(\psi_2'+v_2')^2dx\Big] = 0 \quad L_1 \le x \le L \end{cases} \tag{57}$$

It is further simplified by using the static equations of motion in Eq. (52) and by only retaining the linear terms in $v_i(x,t)$:

$$\begin{cases} \frac{\rho A}{EI}\ddot{v}_1 + v_1'''' + \lambda^2 v_1'' - \frac{A}{2IL}\psi_1''\Big[\int_0^{L_1}\psi_1' v_1' dx + \int_{L_1}^{L}\psi_2' v_2' dx\Big] = 0 \quad 0 \le x \le L_1 \\ \\ \frac{\rho A}{EI}\ddot{v}_2 + v_2'''' + \lambda^2 v_2'' - \frac{A}{2IL}\psi_2''\Big[\int_0^{L_1}\psi_1' v_1' dx + \int_{L_1}^{L}\psi_2' v_2' dx\Big] = 0 \quad L_1 \le x \le L \end{cases} \tag{58}$$

Let $v_i(x,t) = \phi_i(x)e^{j\omega t}$, $\alpha = \lambda^2$, and $\beta = \frac{\rho A\omega^2}{EI}$. Based on Eq. (58), the mode shape will be represented by a homogeneous solution and a particular solution, with the entire mode shape taking the form of

$$\phi_i(x) = B_1 \sinh s_1 x + B_2 \cosh s_1 x + B_3 \sin s_2 x + B_4 \cos s_2 x + B_5 \psi_i''(x) \tag{59}$$

where $s_{1,2} = \sqrt{\frac{\mp\alpha + \sqrt{\alpha^2+4\beta}}{2}}$.

3.4.4 Reduced Order Model

Now that the mode shape about the buckled configuration has been obtained, we can convert our set of partial differential equations into a set of ordinary differential equations. We start by defining the Lagrangian ($\mathcal{L} = T - U$) of the system. We will simplify our notation to denote the static buckled configuration as $\psi(x)$ and the first mode shape as $\phi(x)$ and will not continue the analysis using the two span approach as the buckled configuration and mode shape are now determined.

$$\begin{aligned} \mathcal{L} =& \frac{1}{2}\rho A\int_0^L (\dot{y}+\dot{z})^2 dx + \frac{1}{2}M(\dot{y}(L_1)+\dot{z})^2 - \frac{1}{2}EI\int_0^L y''^2 dx \\ & - \frac{EAL}{2}\Big[-\frac{p}{EA} + \frac{1}{2L}\int_0^L y'^2 dx\Big]^2 - \frac{T_{PDMS}}{2\varepsilon_0\varepsilon_r S}q^2 \\ & - \frac{d_0 + y(L_1)}{2\varepsilon_0 S}q^2 + \frac{\sigma(d_0+y(L_1))}{\varepsilon_0}q - \frac{\sigma^2 S(d_0+y(L_1))}{2\varepsilon_0} \end{aligned} \tag{60}$$

As we are only interested in modeling the first buckling mode, a one-mode approximation for the Galerkin discretization is used. To approximate the dynamic

motion about the first buckled configuration, let

$$y(x,t) = \psi(x) + \phi(x)\eta(t) \tag{61}$$

where $\phi(x)$ is the first buckling mode shape. We now substitute Eq. (61) into Eq. (60) and perform Lagrange's Equation for the variables $\eta(t)$ and $q(t)$.

$$\frac{d}{dt}\frac{\partial \mathcal{L}}{\partial \dot{\eta}} = \rho A \int_0^L \Big(\phi(x)\ddot{\eta} + \ddot{z}\Big)\phi(x)dx + M\Big(\phi(L_1)\ddot{\eta} + \ddot{z}\Big)\phi(L_1) \tag{62}$$

$$\begin{aligned}\frac{\partial \mathcal{L}}{\partial \eta} = &-EI\int_0^L \Big(\psi''(x) + \phi''(x)\eta\Big)\phi''(x)dx + p\int_0^L \Big(\psi'(x) + \phi'(x)\eta\Big)\phi'(x)dx \\ &- \frac{EA}{2L}\int_0^L \Big(\psi' + \phi'\eta\Big)^2 dx \int_0^L \Big(\psi'(x) + \phi'(x)\eta\Big)\phi'(x)dx \\ &- \frac{\phi(L_1)}{2\varepsilon_0 S}q^2 + \frac{\sigma\phi(L_1)}{\varepsilon_0}q - \frac{\sigma^2 S\phi(L_1)}{2\varepsilon_0}\end{aligned} \tag{63}$$

$$\frac{d}{dt}\frac{\partial \mathcal{L}}{\partial \dot{q}} = 0 \tag{64}$$

$$\frac{\partial \mathcal{L}}{\partial q} = -\frac{T_{PDMS}}{\varepsilon_0 \varepsilon_r S}q - \frac{d_0 + \psi(L_1) + \phi(L_1)\eta}{\varepsilon_0 S}q + \frac{\sigma\Big(d_0 + \psi(L_1) + \phi(L_1)\eta\Big)}{\varepsilon_0} \tag{65}$$

We now perform Lagrange's Equations for each variable

$$\begin{aligned}\frac{d}{dt}\frac{\partial \mathcal{L}}{\partial \dot{\eta}} - \frac{\partial \mathcal{L}}{\partial \eta} &= -c\int_0^L \phi^2(x)\dot{\eta}dx \\ \frac{d}{dt}\frac{\partial \mathcal{L}}{\partial \dot{q}} - \frac{\partial \mathcal{L}}{\partial q} &= -R\dot{q}\end{aligned} \tag{66}$$

where the terms on the RHS of Eq. (66) are the generalized forces for η and q and represent the mechanical and electrical damping respectively.

Substituting Eqs. (62) to (65) into Eq. (66), we arrive at a coupled set of differential equations with respect to $\eta(t)$ and $q(t)$.

$$\begin{aligned} &M_1\ddot{\eta} + M_Z\ddot{z} + D_1\dot{\eta} + K_L\eta + K_Q\eta^2 + K_C\eta^3 + N + \alpha_1 q^2 + \alpha_2 q + \alpha_3 = 0 \\ &\dot{q} = -\frac{q}{\varepsilon_0 SR}\Big[\frac{T_{PDMS}}{\varepsilon_r} + d_0 + \psi(L_1) + \phi(L_1)\eta\Big] + \frac{\sigma\Big(d_0 + \psi(L_1) + \phi(L_1)\eta\Big)}{\varepsilon_0 R} \end{aligned} \tag{67}$$

where

$$\begin{aligned} M_1 &= \rho A\int_0^L \phi^2(x)dx + M\phi^2(L_1) \\ M_Z &= \rho A\int_0^L \phi(x)dx + M\phi(L_1) \\ D_1 &= c\int_0^L \phi^2(x)dx \\ K_L &= EI\int_0^L \phi''^2(x)dx - p\int_0^L \phi'^2(x)dx + \frac{EA}{L}\Big(\int_0^L \psi'(x)\phi'(x)dx\Big)^2 \\ &\quad + \frac{EA}{2L}\int_0^L \psi'^2(x)dx\int_0^L \phi'^2(x)dx \\ K_Q &= \frac{3EA}{2L}\int_0^L \phi'^2(x)dx\int_0^L \psi'(x)\phi'(x)dx \\ K_C &= \frac{EA}{2L}\Big(\int_0^L \phi'^2(x)dx\Big)^2 \\ N &= EI\int_0^L \psi''(x)\phi''dx - p\int_0^L \psi'(x)\phi'dx \\ &\quad + \frac{EA}{2L}\int_0^L \psi'^2dx\int_0^L \psi'\phi'dx \\ \alpha_1 &= \frac{\phi(L_1)}{2\varepsilon_0 S} \\ \alpha_2 &= -\frac{\sigma\phi(L_1)}{\varepsilon_0} \\ \alpha_3 &= \frac{\sigma^2 S\phi(L_1)}{2\varepsilon_0} \end{aligned} \tag{68}$$

After dropping the static terms in the mechanical equation, we arrive at the dy-

namic coupled equations.

$$
\begin{aligned}
&M_1\ddot{\eta} + M_Z\ddot{z} + D_1\dot{\eta} + K_L\eta + K_Q\eta^2 + K_C\eta^3 + \alpha_1 q^2 + \alpha_2 q = 0 \\
&\dot{q} = -\frac{q}{\varepsilon_0 SR}\Big[\frac{T_{PDMS}}{\varepsilon_r} + d_0 + \psi(L_1) + \phi(L_1)\eta\Big] + \frac{\sigma\Big(d_0 + \psi(L_1) + \phi(L_1)\eta\Big)}{\varepsilon_0 R}
\end{aligned}
\tag{69}
$$

As we can see from Eqs. (68) and (69), we have a coupled set of differential equations that describe our dynamic system about the buckled configuration. The coupling arises from $\alpha_1 q^2$ and $\alpha_2 q$ in the mechanical equation, and the terms that contain η in the electrical equation.

3.5 Stability Analysis

Before the full impact model is considered and the dynamics of the sensor are investigated, the stability of the system is analyzed. Intuitively, we expect to see that this system has three equilibrium positions, with two of those being stable and one being unstable showing a pitchfork bifurcation. As the stability of this system is only dependent on the mechanical terms, we will neglect the electrical terms, and the electrical differential equation. After removing the forcing and damping terms, we arrive at the Jacobian of the system.

$$
J = \begin{bmatrix} -\lambda_1 & 1 \\ -\frac{K_L}{M_1} - \frac{2K_Q}{M_1}\eta_{eq} - \frac{3K_C}{M_1}\eta_{eq}^2 & -\lambda_1 \end{bmatrix} \tag{70}
$$

where the η_{eq} terms are determined by finding the equilibrium points from the mechanical equilibrium equation ($K_L\eta_{eq} + K_Q\eta_{eq}^2 + K_C\eta_{eq}^3 = 0$). By analyzing the Jacobian, one can see two stable solutions and one unstable solutions. We now compare the approximated equilibrium profiles of the beam with the exact solution obtained from Section 3.4.2, see Fig. 14a. As deduced from this figure, the approximate solution using one mode is close to the exact solution, but has small deviations in predicting the unstable solution.

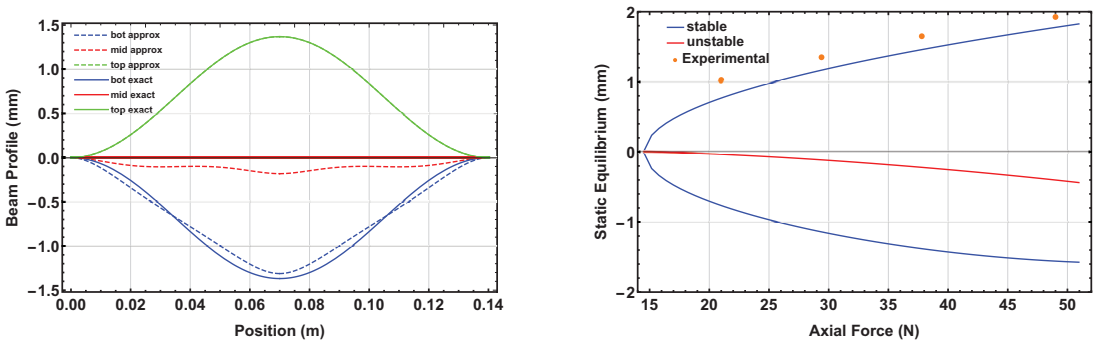

(a) (b)

Figure 14: (a) Comparison between exact equilibrium beam profiles and the approximated one from the one-mode Galerkin Decomposition, (b) Bifurcation diagram for the threshold sensor. Saddle node bifurcation is result of only considering one mode in the Galerkin Decomposition

If we repeat this procedure with different axial forces, we can create a bifurcation diagram for the system, with the axial force being the tuning parameter. From the bifurcation diagram, Fig. 14b, one sees that in addition to the pitchfork bifurcation, there is a saddle node bifurcation where the middle and bottom solutions will eventually collide and destroy each other. Ideally, there should only be a pitchfork bifurcation, but because we are only considering one mode, we are limiting the accuracy of the dynamic system [67]. However, if the axial force is not too large, the one mode solution will be a good approximation.

3.6 Impact Model

Before the full dynamics of the system can be explored, the impact model has to be considered. Using impact equations from [13, 26] and adding the quadratic and cubic stiffness terms, we have

$$F_s = k_i\eta + k_i g_i + K_Q g_i^2 + K_C g i^3 \tag{71a}$$

$$F_d = c_i\eta \tag{71b}$$

We can now represent the full dynamic equations of motion for the free motion and the impact by using a piecewise function, with the condition being whether

the upper electrode is contacting the PDMS layer.

$$\begin{cases} M_1\ddot{\eta} + M_Z\ddot{z} + D_1\dot{\eta} + K_L\eta + K_Q\eta^2 + K_C\eta^3 + \alpha_1 q^2 + \alpha_2 q = 0 & y(L_1,t) > -g_i \\ M_1\ddot{\eta} + M_Z\ddot{z} + (D_1 + c_i)\dot{\eta} + (K_L + k_i)\eta + k_i g_i + K_Q g_i^2 & \\ \qquad + K_C g_i^3 + \alpha_1 q^2 + \alpha_2 q = 0 & y(L_1,t) \leq -g_i \end{cases} \tag{72}$$

where g_i is the gap between the upper electrode and the PDMS layer. It is noted that the total initial gap, d_0, is the summation of g_i, and the penetration distance δ_1.

3.7 Experimental Setup

To experimentally test the concept of the shock sensor, the system was placed on an electrodynamic shaker. A figure of the experimental setup and the block diagram is shown in Fig. 15. The input signal to the shaker was controlled in a closed loop with PUMA Spectral Dynamics. Once the signal was generated, the signal was sent through a power amplifier (Techron 5530 Power Supply Amplifier) and then to the shaker. For the excited base to produce a half-sine pulse, the signal to the electrodynamic shaker requires pre and post compensation pulses, Fig. 16a. These compensation pulses can be seen in Fig. 16a as the low amplitude acceleration pulses that occur before and after the main half-sine pulse. The compensation pulses allow the shaker to use more of its stroke and to produce a decent approximation to a drop table test. The input to the shaker was a half-sine wave with a frequency of $38Hz$. An accelerometer (PCB Piezotronics 352A24) was placed on the base of the shaker and the accelerometer signal was used in the feedback control loop. The accelerometer signal was read by a data acquisition device. The voltage was recorded using an oscilloscope (Tektronix MDO3034). The axial force was controlled by adjusting a screw that was fixed to the setup,

and the axial force was measured using a FlexiForce Sensor. The power amplifier that powers the electrodynamic shaker and the PUMA Spectral Dynamics system are not pictured. The system parameters are listed in Table 4.

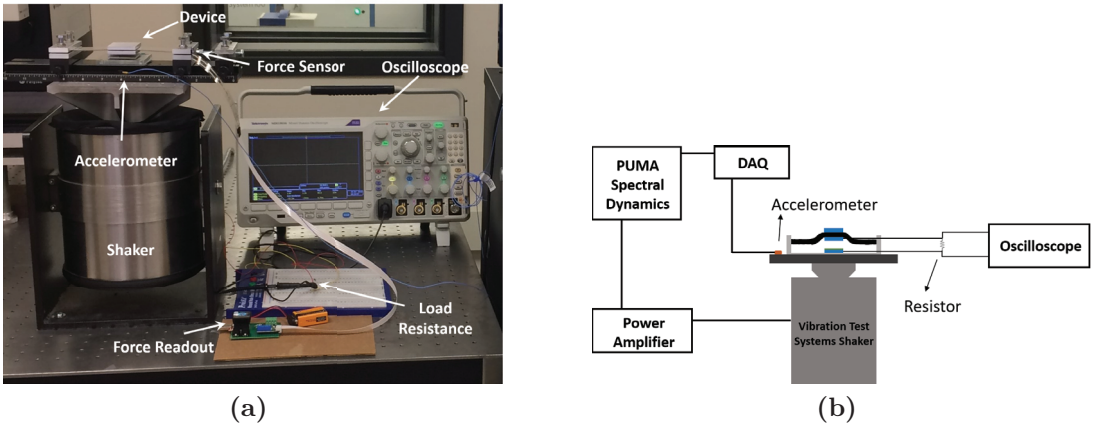

(a) (b)

Figure 15: (a) Picture of the experimental setup, (b) Block diagram of the experimental setup.

3.8 Results and Discussions

Shock simulations were conducted to demonstrate the sensor response when the shock goes beyond the threshold as well as the relationship between the magnitude of the shock signal to the sensed voltage. The results are compared with the data obtained from experiments. We first present a case at an acceleration just below the threshold for this system. The input acceleration measured by an external accelerometer is shown in Fig. 16a. We note that the previously mentioned compensation pulses are not large enough to trigger the switching motion, so these pulses do not affect the system dynamics. We also note that although it looks like the base acceleration pulse and the voltage reading occur at different times, they were recorded at the same time. The difference in time comes from triggering of the oscilloscope. Figs. 16a to 16c show the base acceleration, the simulated voltage output, and the measured voltage output for the low acceleration case. As the threshold acceleration was not reached, the system did not switch states, which is displayed by the lack of a voltage spike. Although it may be obvious, any acceleration amplitudes lower than this low acceleration case will not trigger the system. This design concept regarding bi-stability has the potential to be very

Table 4: Experimental parameters

Parameter	Value
$(L$ x b x $t)$	$(14$ x 3.7 x $0.1)cm$
$(L_m$ x b_m x $t_m)$	$(3.7$ x 5.2 x $0.45)cm$
c	$95\ {}^{Ns}/_{m}$
d_0	$1.3683\ mm$
δ_1	$46.40\ \mu m$
g_i	$1.3219\ mm$
E	$2.344\ GPa$
p	$35\ N$
R	$10\ M\Omega$
T_{PDMS}	$320\ \mu m$
ε_r	2.5
ρ	$1220\ {}^{kg}/_{m^3}$
σ	variable
k_i	$30000\ {}^{N}/_{m}$
c_i	$3000\ {}^{Ns}/_{m}$

reliable because the switching of states can only occur when the threshold acceleration is experienced. Furthermore, even if the sensor experiences an acceleration amplitude greater than the threshold value, but the direction is not in the correct orientation, the device will still not trigger. A sensor that monitors in only one plane at a time could be a drawback in some instances but very useful for systems in which the incoming shock direction is known.

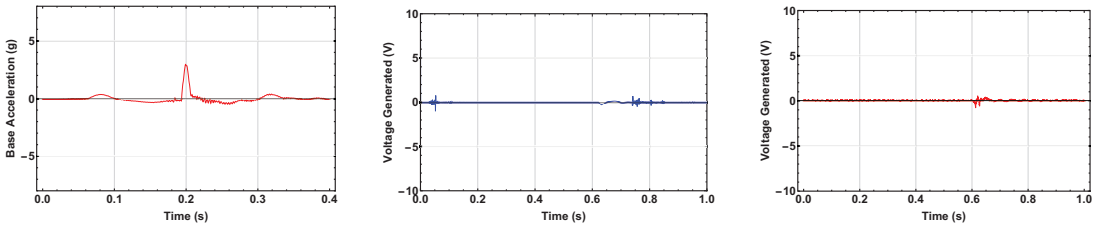

(a) **(b)** **(c)**

Figure 16: (a) Experimental results for the input acceleration pulse at $2.95g$, (b) Simulation of voltage response with shock amplitude of $2.95g$ and $\sigma = 4.2\frac{\mu C}{m^2}$, (c) Experimental voltage results for shock amplitude of $2.95g$

At the threshold acceleration, Fig. 17, there is a significant voltage spike when the sensor experiences input shock. As the upper electrode is switching stable states and moving toward the lower electrode, we see a negative voltage spike. If we compare this threshold case to the previous case in Fig. 16, we see a very

pronounced difference in the voltage outputs. This is one of the main advantages of this specific design, as there is a large signal-to-noise ratio when the device is triggered.

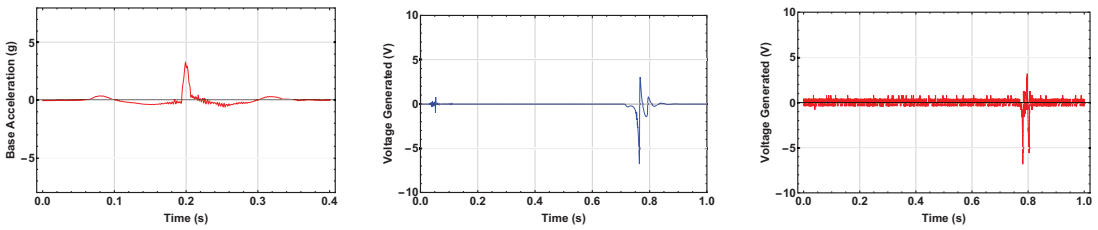

(a) **(b)** **(c)**

Figure 17: (a) Experimental results for the input acceleration pulse at $3.26g$, (b) Simulation of voltage response with shock amplitude of $3.26g$ and $\sigma = 4.2\frac{\mu C}{m^2}$, (c) Experimental voltage results for shock amplitude of $3.26g$

After the initial negative voltage spike, we see a positive voltage spike and then another negative voltage spike. This positive spike is due to an imperfect collision between the upper and lower electrodes. Ideally, when the electrodes come in contact with each other, the velocity of the upper electrode would immediately drop to zero and would remain at a constant zero velocity. But in reality, the upper electrode will start to rebound off of the lower electrode and impact again, which is why we see the positive spike followed by another negative spike. When we discuss the voltage peak for the experimental data we will be referring to the negative voltage peak, as this peak is the first to occur and has the greatest magnitude. To further illustrate the relationship between the mechanical motion and the electrical output, we present Fig. 18a, which displays the displacement and velocity of the upper electrode (beam midspan) once the shock pulse is felt. Fig. 18b displays the charge transferred between the electrodes and the voltage across the load when the shock pulse is felt. Figs. 18a and 18b are performed under an acceleration amplitude of $4.56g$. From Fig. 18a, when the upper electrode is crossing through the unstable equilibrium point, the maximum velocity occurs. As the upper electrode moves toward the lower electrode and the velocity changes rapidly, the charge changes quickly. This change in charge results in the negative voltage spike. Once the impact occurs, the velocity dramatically decreases in magnitude and the upper electrode rebounds slightly apart from the lower electrode

and then impacts again. This small deviation is what causes the positive and second negative peak. After these three voltage peaks have occurred, the system settles into a state of equilibrium between all of these quantities.

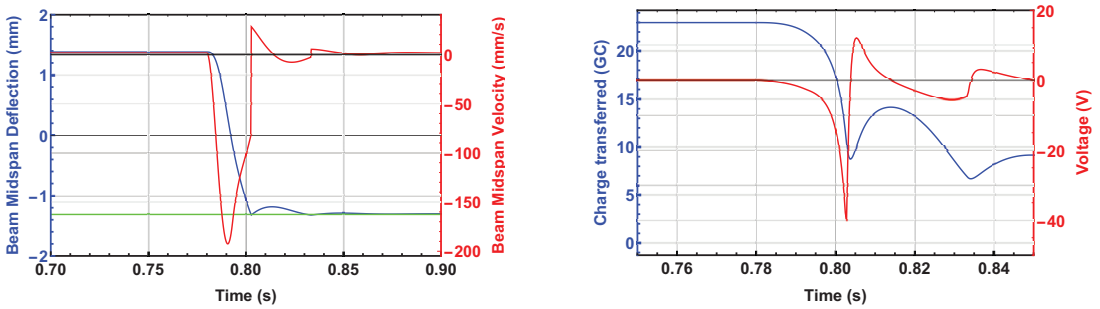

Figure 18: (a) Position and velocity of beam midspan for acceleration amplitude of 4.56g. The green line represents the position of the PDMS layer on the lower electrode, (b) Charge transferred and voltage output for acceleration amplitude of 4.56g

Next, we increase the input shock amplitude to magnitudes larger than the threshold amplitude. This is to display the characteristic of the shock sensor as an accelerometer beyond the threshold. We not only see a voltage spike that indicates that the threshold acceleration has been reached, but we see a voltage peak that is related to the magnitude of the input shock signal. As we expect to see, as the input shock amplitude increases, we see a larger negative voltage peak. These results are displayed in Figs. 19 and 20. We see that there is a close agreement in the simulation and experimental results on the negative voltage spike that occurs from switching between the two stable states. It is noted that the the surface charge density used in simulations is identified from experiments, which shows its increase from increasing the shock level. The reason is the stronger impact causes larger penetration into the PDMS layer [12], hence, more charges are generated on the contact surfaces resulting in larger surface charge density.

At last, the relationship between the input acceleration magnitude and the output voltage peak is demonstrated, see Fig. 21. Again, for the output voltage signal, we are just considering the magnitude of the negative voltage spike, as that is the voltage associated with the input shock signal. It is deduced that the sensor has zero output below the threshold shock of 3.26g, and its voltage

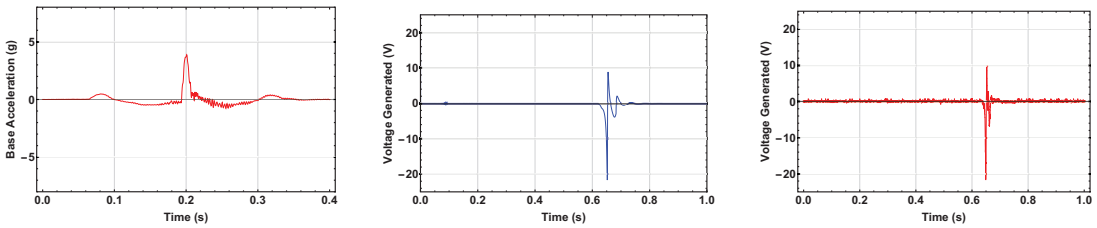

(a) (b) (c)

Figure 19: (a) Experimental results for the input acceleration pulse at $3.88g$, (b) Simulation of voltage response with shock amplitude of $3.88g$ and $\sigma = 10.5\frac{\mu C}{m^2}$, (c) Experimental voltage results for shock amplitude of $3.88g$

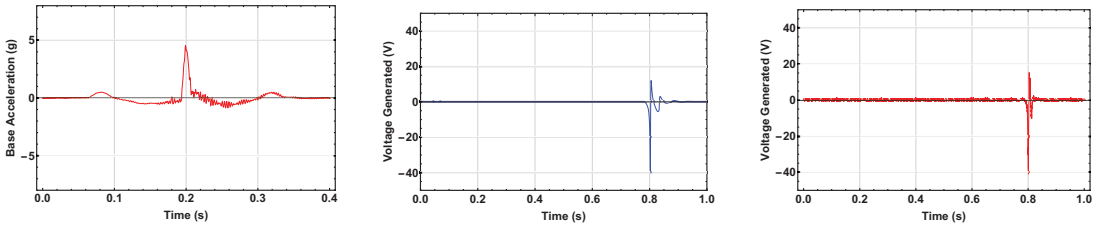

(a) (b) (c)

Figure 20: (a) Experimental results for the input acceleration pulse at $4.56g$, (b) Simulation of voltage response with shock amplitude of $4.56g$ and $\sigma = 12.5\frac{\mu C}{m^2}$, (c) Experimental voltage results for shock amplitude of $4.56g$

output is fairly linearly proportional to the acceleration beyond the threshold as seen in Fig. 21. Although some of these voltage peaks are not monotonically increasing with the acceleration amplitude, Fig. 21 still shows that there is a general linear trend between input acceleration and voltage. As this idea is only a proof of concept, future work will be done to address the slight variations in the voltage amplitude. The results indicate the addition of a buckling mechanism to the triboelectric generator enables a threshold shock sensor that responds to accelerations beyond a threshold. In addition, the proportionality of the output voltage to the acceleration beyond the threshold reveals that a threshold sensor can effectively be used as an accelerometer. This characterization effort is an important part of the sensor development that can be completed by adding an electrical readout.

3.9 Conclusions

A proposed design and proof of concept of a bi-stable threshold sensor using triboelectric transduction was investigated. A continuous model using nonlinear

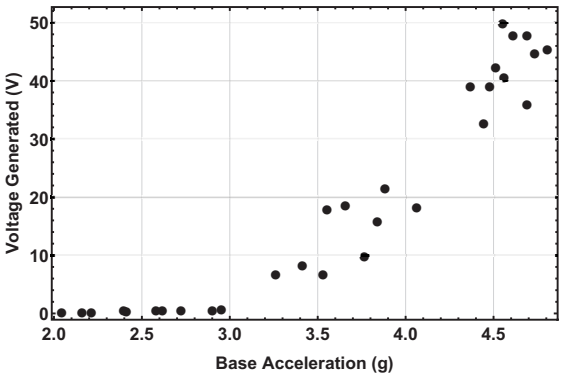

Figure 21: Experimental output voltages of the sensor as a function of shock accelerations. A simple linear fit is used to characterize the linearity of the relationship between voltage and shock amplitude.

Euler-Bernoulli beam theory was derived to accurately describe the system behavior. The model proved to accurately capture the system dynamics as well as output voltages observed experimentally. This presented sensor was not only able to display a significant voltage reading when the acceleration meets or exceeds a threshold, but it was also able to relate the amplitude of the input shock signal to the output voltage amplitude. This is advantageous as the user would be able to know how much of a shock the device experienced during the triggering and not just that the device was triggered. This device also can be tuned by adjusting the axial force that will determine the buckling level of the beam. Increasing the axial force enhances the sensor robustness and increases the threshold shock it can detect. This capability enables a tunable shock sensor. For the parameters that were used this study, we were able to trigger the device at fairly low g-levels ($3.26g$), which can be very useful for low shock level applications. Although this specific sensor is not on the micro-scale, the fundamental understanding of the system behavior and its characterization are useful for the future development of a miniature counterpart.

4 Conclusion

Two uses for triboelectric generators were presented. The tunable wideband energy harvester displayed its advantages compared to linear harvesters. The tunability was implemented by including a compressive axial force in the system. This allowed the harvester to accommodate different frequency sources. Although the system had to be statically tuned, the harvester was still self powered. The operating bandwidth was increased by adding an amplitude limiter to the system. The amplitude limiter made use of the constant contact and separation that is characteristic of the triboelectric effect. Because of the amplitude limiter, the impact between triboelectric materials was able to occur at frequencies that were far away from the natural frequency. Since the impact results in higher voltages than in the free vibration case, the impact over a large range of frequencies resulted in a large operating bandwidth for the system. The axial force was not only able to shift the natural frequency, but was also able to allow for higher voltage outputs due to the softening effect that the axial force had on the system.

A proof of concept for a bi-stable threshold sensor using triboelectric transduction was proposed. This system was completely self powered and was able to reliably generate a voltage signal when the threshold acceleration was met. The reliability of this device is due to the buckling phenomenon. Since the clamped-clamped beam is buckled, the system will only switch states when at least the threshold acceleration is experienced. At acceleration magnitudes lower than the threshold, the system will stay in the upper stable position and there will be no voltage signal. Once the threshold acceleration is felt, the strength of the impact and therefore the voltage magnitude is related to the level of the shock acceleration. This is valuable because many threshold sensors do not give any information except that the threshold has been reached. In this way, after the threshold accel-

eration has been met, the system acts like an accelerometer. This proof of concept is ideal for systems in which the direction of the shock input is known. This is because the system will only trigger at the threshold if the entire shock input is in the same direction as the transverse motion.

Future work will be done to validate the wideband harvester model with the addition of the axial force. The preliminary experimental data had the same characteristics to the model, but the fit was not close enough to validate the model. Concerning the threshold sensor, the effect of gravity could be accounted for in the dynamics. The variations in the output voltage in Fig. 21 could also be addressed to create a more consistent characterization between output voltage and input shock amplitude.

5 Appendix

5.1 Mathematica Codes

5.1.1 Wideband Energy Harvester Code

```
Wideband Energy Harvester

Define Parameter for the System

ClearAll["Global‘*"];
b = 3.7*^-2;
h = 1*^-3;
L = 11*^-2;
bm = 0.052;
Lm = 0.037;


rhomass = 2700;
rho = 1220;

L1 = L/2;
LL = (L - Lm)/2;
LR = LL + Lm;


EEp = 2.344*^9;
EEa = 69*^9;

Ap = b h;
Aa = bm hm;
IIp = (b h^3)/12;


hm1 = 0.00475;
hm2 = 0.00475;


Db = EEa bm (hm1^3/3 + (h hm1^2)/2 + (h^2 hm1)/4) + EEp IIp +
   EEa bm (hm2^3/3 + (h hm2^2)/2 + (h^2 hm2)/4);
rhoA = rho Ap + rhomass bm hm1 + rhomass bm hm2;


ep0 = 8.85*^-12;

S = bm Lm;
Tpdms = 500*^-6;
epr = 2.5;
d0 = 260*^-6;
```

```
g = 9.81;
Amp = 0.5*g;
R = 2*^6;
gi = d0 - 10*^-6;



Mode Shape Analysis

Define the Axial Force Here:

p = 0;
pvec = {p};
wvec = Range[1, 2000, 1];
vec = ConstantArray[0, Length[wvec]];

For[jj = 1, jj <= Length[wvec], jj++,

  ww = wvec[[jj]];
  beta1 = ((rho Ap ww^2)/(EEp IIp));
  beta1a = p/(EEp IIp);
  beta2 = ((rhoA ww^2)/Db);
  beta2a = p/Db;
  r11 = Sqrt[(-beta1a + Sqrt[beta1a^2 + 4 beta1])/2] // N;
  r12 = Sqrt[(beta1a + Sqrt[beta1a^2 + 4 beta1])/2] // N;
  r21 = Sqrt[(-beta2a + Sqrt[beta2a^2 + 4 beta2])/2] // N;
  r22 = Sqrt[(beta2a + Sqrt[beta2a^2 + 4 beta2])/2] // N;
  phi1[x_] =
   A1 (Cosh[r11 x] - Cos[r12 x]) + B1 (Sinh[r11 x] - r11/r12 Sin[r12 x]) // N;
  phi2[x_] =
   A2 Cosh[r21 x] + B2 Sinh[r21 x] + C2 Cos[r22 x] + D2 Sin[r22 x] // N;
  phi3[x_] =
   A3 Cosh[r11 x] + B3 Sinh[r11 x] + C3 Cos[r12 x] + D3 Sin[r12 x] // N;
  eqn3 = phi1[LL] - phi2[LL] == 0 // N;
  eqn4 = phi1'[LL] == 0 // N;
  eqn5 = phi2'[LL] == 0 // N;
  eqn6 = phi2'[LR] == 0 // N;
  eqn7 = phi2[LR] - phi3[LR] == 0 // N;
  eqn8 = phi3'[LR] == 0 // N;
  eqn9 = phi2[LL] - phi2[LR] == 0 // N;
  eqn10 = EEp IIp phi1'''[LL] + Db phi2'''[LR] - Db phi2'''[LL] -
      EEp IIp phi3'''[LR] == 0 // N;
  eqn11 = phi3[L] == 0 // N;
  eqn12 = phi3'[L] == 0 // N;
  eqnvec = {eqn3, eqn4, eqn5, eqn6, eqn7, eqn8, eqn9, eqn10, eqn11, eqn12};
  mat = CoefficientArrays[eqnvec, {A1, B1, A2, B2, C2, D2, A3, B3, C3, D3}][[
     2]] // N;
  vec[[jj]] = Det[mat];
  ];
index = {};
For[ii = 1, ii < Length[vec], ii++,

  If[Sign[vec[[ii]]*vec[[ii + 1]]] == -1, {index = Append[index, ii]}]
  ];
index = index[[1]];
wvec1 = Range[index, index + 1, 0.001];
vec1 = ConstantArray[0, Length[wvec1]];
For[jj = 1, jj <= Length[wvec1], jj++,
```

```
  ww = wvec1[[jj]];
  beta1 = ((rho Ap ww^2)/(EEp IIp));
  beta1a = p/(EEp IIp);
  beta2 = ((rhoA ww^2)/Db);
  beta2a = p/Db;
  r11 = Sqrt[(-beta1a + Sqrt[beta1a^2 + 4 beta1])/2] // N;
  r12 = Sqrt[(beta1a + Sqrt[beta1a^2 + 4 beta1])/2] // N;
  r21 = Sqrt[(-beta2a + Sqrt[beta2a^2 + 4 beta2])/2] // N;
  r22 = Sqrt[(beta2a + Sqrt[beta2a^2 + 4 beta2])/2] // N;
  phi1[x_] =
   A1 (Cosh[r11 x] - Cos[r12 x]) + B1 (Sinh[r11 x] - r11/r12 Sin[r12 x]) // N;
  phi2[x_] =
   A2 Cosh[r21 x] + B2 Sinh[r21 x] + C2 Cos[r22 x] + D2 Sin[r22 x] // N;
  phi3[x_] =
   A3 Cosh[r11 x] + B3 Sinh[r11 x] + C3 Cos[r12 x] + D3 Sin[r12 x] // N;
  eqn3 = phi1[LL] - phi2[LL] == 0 // N;
  eqn4 = phi1'[LL] == 0 // N;
  eqn5 = phi2'[LL] == 0 // N;
  eqn6 = phi2'[LR] == 0 // N;
  eqn7 = phi2[LR] - phi3[LR] == 0 // N;
  eqn8 = phi3'[LR] == 0 // N;
  eqn9 = phi2[LL] - phi2[LR] == 0 // N;
  eqn10 = EEp IIp phi1'''[LL] + Db phi2'''[LR] - Db phi2'''[LL] -
      EEp IIp phi3'''[LR] == 0 // N;
  eqn11 = phi3[L] == 0 // N;
  eqn12 = phi3'[L] == 0 // N;
  eqnvec = {eqn3, eqn4, eqn5, eqn6, eqn7, eqn8, eqn9, eqn10, eqn11, eqn12};
  mat = CoefficientArrays[eqnvec, {A1, B1, A2, B2, C2, D2, A3, B3, C3, D3}][[
     2]] // N;
  vec1[[jj]] = Det[mat];
  ];
zerosapprox = {};
index1 = {};
For[ii = 1, ii < Length[vec1], ii++,
   If[Sign[vec1[[ii]]*vec1[[ii + 1]]] == -1, {zerosapprox =
      Append[zerosapprox, (vec1[[ii]] + vec1[[ii + 1]])/2],
     index1 = Append[index1, ii]}]
   ] // Quiet;
index1 = index1[[1]];
w1 = wvec1[[index1]]
f1 = w1/2/Pi

Clear[ww];
beta1 = ((rho Ap ww^2)/(EEp IIp)) /. ww -> w1;
beta1a = p/(EEp IIp);
beta2 = ((rhoA ww^2)/Db) /. ww -> w1;
beta2a = p/Db;
r11 = Sqrt[(-beta1a + Sqrt[beta1a^2 + 4 beta1])/2] // N;
r12 = Sqrt[(beta1a + Sqrt[beta1a^2 + 4 beta1])/2] // N;
r21 = Sqrt[(-beta2a + Sqrt[beta2a^2 + 4 beta2])/2] // N;
r22 = Sqrt[(beta2a + Sqrt[beta2a^2 + 4 beta2])/2] // N;
phi1[x_] =
  A1 (Cosh[r11 x] - Cos[r12 x]) + B1 (Sinh[r11 x] - r11/r12 Sin[r12 x]) // N;
phi2[x_] =
  A2 Cosh[r21 x] + B2 Sinh[r21 x] + C2 Cos[r22 x] + D2 Sin[r22 x] // N;
phi3[x_] =
  A3 Cosh[r11 x] + B3 Sinh[r11 x] + C3 Cos[r12 x] + D3 Sin[r12 x] // N;
```

```
eqn3 = phi1[LL] - phi2[LL] == 0 // N;
eqn4 = phi1'[LL] == 0 // N;
eqn5 = phi2'[LL] == 0 // N;
eqn6 = phi2'[LR] == 0 // N;
eqn7 = phi2[LR] - phi3[LR] == 0 // N;
eqn8 = phi3'[LR] == 0 // N;
eqn9 = phi2[LL] - phi2[LR] == 0 // N;
eqn10 = EEp IIp phi1'''[LL] + Db phi2'''[LR] - Db phi2'''[LL] -
     EEp IIp phi3'''[LR] == 0 // N;
eqn11 = phi3[L] == 0 // N;
eqn12 = phi3'[L] == 0 // N;
eqnvec = {eqn3, eqn4, eqn5, eqn6, eqn7, eqn8, eqn9, eqn10, eqn11, eqn12};
mat = CoefficientArrays[eqnvec, {A1, B1, A2, B2, C2, D2, A3, B3, C3, D3}][[
    2]] // N;
matrank = mat;
mateqn = {matrank[[1, All]]};
mattrial = mateqn;
count = 0;

For[ii = 2, ii <= Dimensions[matrank][[1]], ii++,
 mattrial = Join[mattrial, {matrank[[ii, All]]}];
 If[MatrixRank[mattrial] + count == ii,
  mateqn = Join[mateqn, {matrank[[ii, All]]}], {count = count + 1,
   mateqn = mateqn}];
 ]
eqnfrommat = mateqn.{A1, B1, A2, B2, C2, D2, A3, B3, C3, D3};
eqns1 = {eqnfrommat[[1]] == 0, eqnfrommat[[2]] == 0, eqnfrommat[[3]] == 0,
   eqnfrommat[[4]] == 0, eqnfrommat[[5]] == 0, eqnfrommat[[6]] == 0,
   eqnfrommat[[7]] == 0, eqnfrommat[[8]] == 0, eqnfrommat[[9]] == 0};
sol = Flatten[Solve[eqns1, {B1, A2, B2, C2, D2, A3, B3, C3, D3}]];
coeffB1 = B1 /. sol[[1]];
coeffA2 = A2 /. sol[[2]];
coeffB2 = B2 /. sol[[3]];
coeffC2 = C2 /. sol[[4]];
coeffD2 = D2 /. sol[[5]];
coeffA3 = A3 /. sol[[6]];
coeffB3 = B3 /. sol[[7]];
coeffC3 = C3 /. sol[[8]];
coeffD3 = D3 /. sol[[9]];
phi1[x_] =
  phi1[x] /. {B1 -> coeffB1, A2 -> coeffA2, B2 -> coeffB2, C2 -> coeffC2,
    D2 -> coeffD2, A3 -> coeffA3, B3 -> coeffB3, C3 -> coeffC3, D3 -> coeffD3};
phi2[x_] =
  phi2[x] /. {B1 -> coeffB1, A2 -> coeffA2, B2 -> coeffB2, C2 -> coeffC2,
    D2 -> coeffD2, A3 -> coeffA3, B3 -> coeffB3, C3 -> coeffC3, D3 -> coeffD3};
phi3[x_] =
  phi3[x] /. {B1 -> coeffB1, A2 -> coeffA2, B2 -> coeffB2, C2 -> coeffC2,
    D2 -> coeffD2, A3 -> coeffA3, B3 -> coeffB3, C3 -> coeffC3, D3 -> coeffD3};
phitot[x_] = If[x <= LL, phi1[x], If[x > LL && x <= LR, phi2[x], phi3[x]]];
coeffA1 = A1 /.
   Solve[Integrate[rho Ap phitot[x]^2, {x, 0, LL}] +
       Integrate[rhoA phitot[x]^2, {x, LL, LR}] +
       Integrate[rho Ap phitot[x]^2, {x, LR, L}] == 1, A1][[2]];
(*coeffA1=1;*)
phi1[x_] = phi1[x] /. {A1 -> coeffA1};
phi2[x_] = phi2[x] /. {A1 -> coeffA1};
phi3[x_] = phi3[x] /. {A1 -> coeffA1};
phitot[x_] = phitot[x];
```

```
Plot[phitot[x], {x, 0, L}, Frame -> True,
 FrameLabel -> {"Position (m)", "Modeshape"}, ImageSize -> Large,
 PlotRange -> All, BaseStyle -> {FontWeight -> "Bold", FontSize -> 20},
 PlotStyle -> {Black, Thick}, FrameStyle -> Directive[Thick, Black, Bold],
 FrameTicksStyle -> Black, GridLines -> Automatic]
Print["The first natural frequency with the center mass and no axial force \
is: ", f1, " Hz"];

Reduced Order Model and Impact Coefficients

M1 = rho Ap NIntegrate[phi1[x]^2, {x, 0, LL}] +
   rhoA NIntegrate[phi2[x]^2, {x, LL, LR}] +
   rho Ap NIntegrate[phi3[x]^2, {x, LR, L}];
MZ = rho Ap NIntegrate[phi1[x], {x, 0, LL}] +
   rhoA NIntegrate[phi2[x], {x, LL, LR}] +
   rho Ap NIntegrate[phi3[x], {x, LR, L}];
KL = EEp IIp NIntegrate[phi1''[x]^2, {x, 0, LL}] +
   Db NIntegrate[phi2''[x]^2, {x, LL, LR}] +
   EEp IIp NIntegrate[phi3''[x]^2, {x, LR, L}] -
   p NIntegrate[phi1'[x]^2, {x, 0, LL}] -
   p NIntegrate[phi2'[x]^2, {x, LL, LR}] -
   p NIntegrate[phi3'[x]^2, {x, LR, L}];

Define Damping Constant

c = 52;
D1 = c NIntegrate[phi1[x]^2, {x, 0, LL}] +
   c NIntegrate[phi2[x]^2, {x, LL, LR}] + c NIntegrate[phi3[x]^2, {x, LR, L}];

sigma = 3.2*^-6;

alpha1 = -phitot[L1]/(2 ep0 S);
alpha2 = (sigma phitot[L1])/ep0;


ci = 5000;
ki = 2000;

define values

freqL = 10*2*\[Pi];
freqH = 60*2*\[Pi];
npoints = (freqH - freqL)/(2 Pi)*1;
stepsize = (freqH - freqL)/npoints;
freq = Range[freqL, freqH, stepsize];

period = (2 \[Pi])/freq;
\[Eta]1 = 0;
\[Eta]2 = 0;
\[Eta]3 = 0;

xx1 = ConstantArray[0, 1000];
xx2 = ConstantArray[0, 1000];
xx3 = ConstantArray[0, 1000];
xx4 = ConstantArray[0, 1000];
xx5 = ConstantArray[0, 1000];
xx6 = ConstantArray[0, 1000];
```

```
xx7 = ConstantArray[0, 1000];
xx8 = ConstantArray[0, 1000];
xx9 = ConstantArray[0, 1000];
xx10 = ConstantArray[0, 1000];
xx11 = ConstantArray[0, 1000];
xx12 = ConstantArray[0, 1000];
DDq = ConstantArray[0, 1000];
DDxx2 = ConstantArray[0, 1000];
e1 = 1;
e2 = 1;
e3 = 1;

tol1 = 1*^-8;
tol2 = 1*^-6;
tol3 = 1*^-13;
ifbreak = 0;

stable = ConstantArray[Null, {Length[freq], 2}];
unstable = ConstantArray[Null, {Length[freq], 2}];



frequency response

timebeg = AbsoluteTime[];
For[kk = 1, kk <= 1, kk++,
  (*kk = 1 is a forward sweep, kk = 2 is a backward sweep*)
  If[kk == 1, freq = Range[freqL, freqH, stepsize],
   freq = Range[freqH, freqL, -stepsize]];
  period = (2 \[Pi])/freq;

  For[ii = 1, ii <= Length[freq], ii++,
   ifbreak = 0;

   If[ii ==
     1, {\[Eta]1 = 0, \[Eta]2 = 0, \[Eta]3 =
      0}, {\[Eta]1 = \[Eta]1, \[Eta]2 = \[Eta]2, \[Eta]3 = \[Eta]3}];

   Print[freq[[ii]]/( 2 \[Pi]) // N];

   e1 = 1;
   e2 = 1;
   e3 = 1;
   check1 = 1;
   check2 = 1;
   check3 = 1;
   jj = 1;

   While[check1 + check2 + check3 > 0,
    Off[General::stop];

    eqns = {x1'[t] == x2[t],
      x2'[t] ==
       Piecewise[{{-1/
           M1 (MZ Amp Cos[freq[[ii]] t] + D1 x2[t] + KL x1[t] +
             alpha1 x3[t]^2 + alpha2 x3[t]),
          x1[t] phitot[L1] < gi}, {-1/
           M1 (MZ Amp Cos[freq[[ii]] t] + D1 x2[t] + ci x2[t] + KL x1[t] +
```

```
        ki x1[t] - ki gi + alpha1 x3[t]^2 + alpha2 x3[t]),
      x1[t] phitot[L1] >= gi}}],
  x3'[t] == -x3[t]/(ep0 S R) (Tpdms/epr + d0 - phitot[L1] x1[t]) + (
    sigma (d0 - phitot[L1] x1[t]))/(ep0 R),
  x4'[t] == x7[t],
  x5'[t] == x8[t],
  x6'[t] == x9[t],
  x7'[t] ==
   Piecewise[{{-1/
       M1 (D1 x7[t] + KL x4[t] + 2 alpha1 x10[t] x3[t] + alpha2 x10[t]),
      x1[t] phitot[L1] < gi}, {-1/
       M1 (D1 x7[t] + ci x7[t] + KL x4[t] + ki x4[t] +
         2 alpha1 x10[t] x3[t] + alpha2 x10[t]), x1[t] phitot[L1] >= gi}}],
  x8'[t] ==
   Piecewise[{{-1/
       M1 (D1 x8[t] + KL x5[t] + 2 alpha1 x11[t] x3[t] + alpha2 x11[t]),
      x1[t] phitot[L1] < gi}, {-1/
       M1 (D1 x8[t] + ci x8[t] + KL x5[t] + ki x5[t] +
         2 alpha1 x11[t] x3[t] + alpha2 x11[t]), x1[t] phitot[L1] >= gi}}],
  x9'[t] ==
   Piecewise[{{-1/
       M1 (D1 x9[t] + KL x6[t] + 2 alpha1 x12[t] x3[t] + alpha2 x12[t]),
      x1[t] phitot[L1] < gi}, {-1/
       M1 (D1 x9[t] + ci x9[t] + KL x6[t] + ki x6[t] +
         2 alpha1 x12[t] x3[t] + alpha2 x12[t]), x1[t] phitot[L1] >= gi}}],
  x10'[t] == (-x10[t] Tpdms)/(ep0 S R epr) - (x10[t] d0)/(ep0 S R) + (
    x3[t] phitot[L1] x4[t])/(ep0 S R) + (x10[t] phitot[L1] x1[t])/(
    ep0 S R) - (sigma phitot[L1] x4[t])/(ep0 R),
  x11'[t] == (-x11[t] Tpdms)/(ep0 S R epr) - (x11[t] d0)/(ep0 S R) + (
    x3[t] phitot[L1] x5[t])/(ep0 S R) + (x11[t] phitot[L1] x1[t])/(
    ep0 S R) - (sigma phitot[L1] x5[t])/(ep0 R),
  x12'[t] == (-x12[t] Tpdms)/(ep0 S R epr) - (x12[t] d0)/(ep0 S R) + (
    x3[t] phitot[L1] x6[t])/(ep0 S R) + (x12[t] phitot[L1] x1[t])/(
    ep0 S R) - (sigma phitot[L1] x6[t])/(ep0 R)
  };

init = {x1[0] == \[Eta]1, x2[0] == \[Eta]2, x3[0] == \[Eta]3, x4[0] == 1,
  x5[0] == 0, x6[0] == 0, x7[0] == 0, x8[0] == 1, x9[0] == 0, x10[0] == 0,
   x11[0] == 0, x12[0] == 1};

sol = Flatten[
  NDSolve[{eqns, init}, {x1, x2, x3, x4, x5, x6, x7, x8, x9, x10, x11,
    x12}, {t, period[[ii]]},
   Method -> {"DiscontinuityProcessing" -> False}, MaxSteps -> Infinity]];
{tstart, tstop} = Flatten[x1["Domain"] /. sol] // N;
periodcheck = period[[ii]] // N;
If[Not[
  periodcheck ===
   tstop], {\[Eta]1 = \[Eta]1/4, \[Eta]2 = \[Eta]2/4, \[Eta]3 = \[Eta]3/4,
   ifbreak = 1}];
If[ifbreak == 1, Break[]];

X1[t_] = x1[t] /. sol;
X2[t_] = x2[t] /. sol;
X3[t_] = x3[t] /. sol;
X4[t_] = x4[t] /. sol;
X5[t_] = x5[t] /. sol;
X6[t_] = x6[t] /. sol;
```

```
X7[t_] = x7[t] /. sol;
X8[t_] = x8[t] /. sol;
X9[t_] = x9[t] /. sol;
X10[t_] = x10[t] /. sol;
X11[t_] = x11[t] /. sol;
X12[t_] = x12[t] /. sol;

Dq[t_] = D[X3[t], t];
Dxx2[t_] = D[X2[t], t];
For[gg = 1, gg <= 1000, gg++,

 xx1[[gg]] = X1[gg/1000 period[[ii]]];
 xx2[[gg]] = X2[gg/1000 period[[ii]]];
 xx3[[gg]] = X3[gg/1000 period[[ii]]];
 xx4[[gg]] = X4[gg/1000 period[[ii]]];
 xx5[[gg]] = X5[gg/1000 period[[ii]]];
 xx6[[gg]] = X6[gg/1000 period[[ii]]];
 xx7[[gg]] = X7[gg/1000 period[[ii]]];
 xx8[[gg]] = X8[gg/1000 period[[ii]]];
 xx9[[gg]] = X9[gg/1000 period[[ii]]];
 xx10[[gg]] = X10[gg/1000 period[[ii]]];
 xx11[[gg]] = X11[gg/1000 period[[ii]]];
 xx12[[gg]] = X12[gg/1000 period[[ii]]];
 DDq[[gg]] = Dq[gg/1000 period[[ii]]];
 DDxx2[[gg]] = Dxx2[gg/1000 period[[ii]]];
 ];


mat1 = ( {
    {Last[xx4], Last[xx5], Last[xx6]},
    {Last[xx7], Last[xx8], Last[xx9]},
    {Last[xx10], Last[xx11], Last[xx12]}
   } ) - IdentityMatrix[3];
mat2 = ( {
   {\[Eta]1 - Last[xx1]},
   {\[Eta]2 - Last[xx2]},
   {\[Eta]3 - Last[xx3]}
  } );
dev = LinearSolve[mat1, mat2];

e1 = dev[[1, 1]];
e2 = dev[[2, 1]];
e3 = dev[[3, 1]];
If[Abs[e1] > tol1, check1 = 1, check1 = 0];
If[Abs[e2] > tol2, check2 = 1, check2 = 0];
If[Abs[e3] > tol3, check3 = 1, check3 = 0];
\[Eta]1 = \[Eta]1/1 + e1/4;
\[Eta]2 = \[Eta]2/1 + e2/4;
\[Eta]3 = \[Eta]3/1 + e3/4;

jj = jj + 1;

If[jj >= 50, {check1 = 0, check2 = 0, check3 = 0}]
];

If[ifbreak == 0, {
 maxval = 0;
```

```
      For[qq = 1, qq <= Length[DDq], qq++,

       If[R*DDq[[qq]] >= maxval, {maxval = R* DDq[[qq]], tpos = qq}];

       ];

      mandmatrix = ( {
         {Last[xx4], Last[xx5], Last[xx6]},
         {Last[xx7], Last[xx8], Last[xx9]},
         {Last[xx10], Last[xx11], Last[xx12]}
        } );
      eigs = Abs[Eigenvalues[mandmatrix]];
      eig1 = eigs[[1]];
      eig2 = eigs[[2]];
      eig3 = eigs[[3]];
      If[eig1 < 1 && eig2 < 1 && eig3 < 1, stable[[ii, kk]] = maxval,
       unstable[[ii, kk]] = maxval];}];

   ];

  If[kk == 1, {stabledata1 = Transpose[{freq/(2 \[Pi]), stable[[All, 1]]}],
    unstabledata1 =
     Transpose[{freq/(2 \[Pi]), unstable[[All, 1]]}]}, {stabledata2 =
     Transpose[{freq/(2 \[Pi]), stable[[All, 2]]}],
    unstabledata2 = Transpose[{freq/(2 \[Pi]), unstable[[All, 2]]}]}];
  ];
(AbsoluteTime[] - timebeg)/60

pforward =
 ListLinePlot[{stabledata1},
  PlotRange -> {{freqL/(2 \[Pi]), freqH/(2 \[Pi])}, All}, Frame -> True,
  FrameLabel -> {"Frequency (Hz)", "Voltage Generated (V)"},
  ImageSize -> Large, PlotStyle -> Blue,
  FrameStyle -> Directive[Thick, Black, Bold], FrameTicksStyle -> Black,
  LabelStyle -> Directive[Bold, Black, FontSize -> 20],
  GridLines -> Automatic,
  PlotLegends ->
   Placed[LineLegend[{Style["simulation", 16]}, Spacings -> 0.15], {0.15,
     0.90}]]
```

5.1.2 Threshold Shock Sensor Code

```
Two Part Beam

Buckling Configuration

ClearAll["Global‘*"];
b = 3.7*^-2;
h = 1*^-3;
L = 14*^-2;
L1 = L/2;
rho = 1220;
EE = 2.344*^9;
A = b h;
II = (b h^3)/12;


bm = 0.052;
Lm = 0.037;
hm = 0.0045;
volmass = bm Lm hm;
rhomass = 2700;
M = rhomass volmass*2;
g = 9.81;



psi1[x_] = c1a + c2a x + c3a Cos[\[Lambda] x] + c4a Sin[\[Lambda] x];
psi2[x_] = c1b + c2b x + c3b Cos[\[Lambda] x] + c4b Sin[\[Lambda] x];
eqn1 = psi1[0] == 0;
eqn2 = psi1'[0] == 0;
eqn3 = psi2[L] == 0;
eqn4 = psi2'[L] == 0;
eqn5 = psi1[L1] == psi2[L1];
eqn6 = psi1'[L1] == psi2'[L1];
eqn8 = psi1''[L1] == psi2''[L1];
eqn7 = EE II psi1'''[L1] - EE II  psi2'''[L1] == 0;

mat = CoefficientArrays[{eqn1, eqn2, eqn3, eqn4, eqn5, eqn6, eqn7,
      eqn8}, {c1a, c2a, c3a, c4a, c1b, c2b, c3b, c4b}][[2]] // N;
Plot[Det[mat], {\[Lambda], 0, 100}, PlotRange -> {All, {-100, 100}},
 ImageSize -> Small]
\[Lambda]zero1 = \[Lambda] /. FindRoot[Det[mat] == 0, {\[Lambda], 50}]

\[Lambda] = \[Lambda]zero1;
matrank = mat;
mateqn = {matrank[[1, All]]};
mattrial = mateqn;
count = 0;
MatrixRank[mat];

For[ii = 2, ii <= Dimensions[matrank][[1]], ii++,

 mattrial = Join[mattrial, {matrank[[ii, All]]}];
```

```
 If[MatrixRank[mattrial] + count == ii,
  mateqn = Join[mateqn, {matrank[[ii, All]]}], {count = count + 1,
   mateqn = mateqn}];

 ]

eqnfrommat = mateqn.{c1a, c2a, c3a, c4a, c1b, c2b, c3b, c4b};
eqns1 = {eqnfrommat[[1]] == 0, eqnfrommat[[2]] == 0, eqnfrommat[[3]] == 0,
   eqnfrommat[[4]] == 0, eqnfrommat[[5]] == 0, eqnfrommat[[6]] == 0,
   eqnfrommat[[7]] == 0};
sol = Flatten[Solve[eqns1, {c2a, c3a, c4a, c1b, c2b, c3b, c4b}]] // Chop;

C2a = c2a /. sol;
C3a = c3a /. sol;
C4a = c4a /. sol;
C1b = c1b /. sol;
C2b = c2b /. sol;
C3b = c3b /. sol;
C4b = c4b /. sol;

psi1[x_] =
  psi1[x] /. {c2a -> C2a, c3a -> C3a, c4a -> C4a, c1b -> C1b, c2b -> C2b,
    c3b -> C3b, c4b -> C4b};
psi2[x_] =
  psi2[x] /. {c2a -> C2a, c3a -> C3a, c4a -> C4a, c1b -> C1b, c2b -> C2b,
    c3b -> C3b, c4b -> C4b};

psi1keep[x_] = psi1[x];
psi2keep[x_] = psi2[x];

psitot[x_] = If[x <= L1, psi1[x], psi2[x]];

pcrit = 4 Pi^2 EE II 1/L^2;

pvecnum = 1;
pvec = ConstantArray[0, pvecnum];
wvec = ConstantArray[0, pvecnum];


bottomvec = {};
middlevec = {};
topvec = {};
stableequil = ConstantArray[Null, {3, Length[pvec]}];
unstableequil = ConstantArray[Null, {3, Length[pvec]}];
stableconfig = stableequil;
unstableconfig = unstableequil;



Define axial force


p = pcrit*1.25;
p = 50;
p = 35;


jj = 1;
```

```
Clear[w];
psi1[x_] = psi1keep[x];
psi2[x_] = psi2keep[x];



C1a = c1a /.
   Solve[\[Sqrt](p/(EE II) -  A/(2 L  II) Integrate[psi1'[x]^2, {x, 0, L1}] -
         A/(2 L  II) Integrate[psi2'[x]^2, {x, L1, L}]) == \[Lambda]zero1,
     c1a][[2]];
psi1[x_] = psi1[x] /. {c1a -> C1a};
psi2[x_] = psi2[x] /. {c1a -> C1a};
psitot[x_] = If[x <= L1, psi1[x], psi2[x]];
Plot[psitot[x], {x, 0, L}];

alpha = \[Lambda]zero1^2;
beta = (rho A w^2)/(EE II);
s1 = Sqrt[(-alpha + Sqrt[alpha^2 + 4 beta])/2];
s2 = Sqrt[(alpha + Sqrt[alpha^2 + 4 beta])/2];
phi1[x_] =
  A11 Sinh[s1 x] + B11 Cosh[s1 x] + C11 Sin[s2 x] + D11 Cos[s2 x] +
   E11 psi1''[x];
phi2[x_] =
  A22 Sinh[s1 x] + B22 Cosh[s1 x] + C22 Sin[s2 x] + D22 Cos[s2 x] +
   E22 psi2''[x];
meqn1 = phi1[0] == 0;
meqn2 = phi1'[0] == 0;
meqn3 = phi2[L] == 0;
meqn4 = phi2'[L] == 0;
meqn5 = phi1[L1] == phi2[L1];
meqn6 = phi1'[L1] == phi2'[L1];
meqn7 = phi1''[L1] == phi2''[L1];
meqn8 = -w^2 M phi1[L1] - EE II phi1'''[L1] + EE II phi2'''[L1] == 0;
meqn9 = E11 (beta + A/(L II) Integrate[psi1'[x]*psi1'''[x], {x, 0, L1}]) +
    E22 A/(L II)  Integrate[psi2'[x]*psi2'''[x], {x, L1, L}] +
    A/(L II) Integrate[
      psi1'[x]*D[
        A11 Sinh[s1 x] + B11 Cosh[s1 x] + C11 Sin[s2 x] + D11 Cos[s2 x], {x,
         1}], {x, 0, L1}] +
    A/(L II) Integrate[
      psi2'[x]*D[
        A22 Sinh[s1 x] + B22 Cosh[s1 x] + C22 Sin[s2 x] + D22 Cos[s2 x], {x,
         1}], {x, L1, L}] == 0;
meqn10 = E22 (beta + A/(L II) Integrate[psi2'[x]*psi2'''[x], {x, L1, L}]) +
    E11 A/(L II)  Integrate[psi1'[x]*psi1'''[x], {x, 0, L1}] +
    A/(L II) Integrate[
      psi1'[x]*D[
        A11 Sinh[s1 x] + B11 Cosh[s1 x] + C11 Sin[s2 x] + D11 Cos[s2 x], {x,
         1}], {x, 0, L1}] +
    A/(L II) Integrate[
      psi2'[x]*D[
        A22 Sinh[s1 x] + B22 Cosh[s1 x] + C22 Sin[s2 x] + D22 Cos[s2 x], {x,
         1}], {x, L1, L}] == 0;
mat = CoefficientArrays[{meqn1, meqn2, meqn3, meqn4, meqn5, meqn6, meqn7,
     meqn8, meqn9, meqn10}, {A11, B11, C11, D11, E11, A22, B22, C22, D22,
     E22}][[2]];
```

```
limititeration = 3;
numpts = 1000;
numptsbase = 1000;
For[iii = 1, iii <= limititeration, iii++,
  If[iii == 1,

    matdisc = ConstantArray[0, numpts];
    wvecdisc = ConstantArray[0, numpts];

    For[qq = 1, qq <= Length[matdisc], qq++,

     matdisc[[qq]] = Det[Normal[mat] /. w -> ((300 qq)/numpts)];
     If[matdisc[[qq]] > 0, matdisc[[qq]] = 1, matdisc[[qq]] = -1];
     wvecdisc[[qq]] = (300 qq)/numpts;
     ];

    index = {};
    For[kk = 1, kk < Length[matdisc], kk++,

     If[Sign[matdisc[[kk]]*matdisc[[kk + 1]]] == -1, {index =
        Append[index, kk]}]
     ];

    wapprox = wvecdisc[[index]][[1]] // N;

    ,
    numpts = numpts + numptsbase;
    matdisc = ConstantArray[0, numpts];
    wvecdisc = ConstantArray[0, numpts];

    For[qq = 1, qq <= Length[matdisc], qq++,

     matdisc[[qq]] =
      Det[Normal[mat] /. w -> ((wapprox*0.05 qq)/numpts) + wapprox*0.975];
     If[matdisc[[qq]] > 0, matdisc[[qq]] = 1, matdisc[[qq]] = -1];
     wvecdisc[[qq]] = ((wapprox*0.05 qq)/numpts) + wapprox*0.975;
     ];

    index = {};
    For[kk = 1, kk < Length[matdisc], kk++,

     If[Sign[matdisc[[kk]]*matdisc[[kk + 1]]] == -1, {index =
        Append[index, kk]}]
     ];

    wapprox = wvecdisc[[index]][[1]];
    ];
  ];

wactual = wapprox;
Print["wactual: ", wactual];
wvec[[jj]] = wactual;
```

```
w = wactual;
alpha = \[Lambda]zero1^2;
beta = (rho A w^2)/(EE II);
s1 = Sqrt[(-alpha + Sqrt[alpha^2 + 4 beta])/2];
s2 = Sqrt[(alpha + Sqrt[alpha^2 + 4 beta])/2];
phi1[x_] =
  A11 Sinh[s1 x] + B11 Cosh[s1 x] + C11 Sin[s2 x] + D11 Cos[s2 x] +
   E11 psi1''[x];
phi2[x_] =
  A22 Sinh[s1 x] + B22 Cosh[s1 x] + C22 Sin[s2 x] + D22 Cos[s2 x] +
   E22 psi2''[x];
meqn1 = phi1[0] == 0;
meqn2 = phi1'[0] == 0;
meqn3 = phi2[L] == 0;
meqn4 = phi2'[L] == 0;
meqn5 = phi1[L1] == phi2[L1];
meqn6 = phi1'[L1] == phi2'[L1];
meqn7 = phi1''[L1] == phi2''[L1];
meqn8 = -w^2 M phi1[L1] - EE II phi1'''[L1] + EE II phi2'''[L1] == 0;
meqn9 = E11 (beta + A/(L II) Integrate[psi1'[x]*psi1'''[x], {x, 0, L1}]) +
    E22 A/(L II)  Integrate[psi2'[x]*psi2'''[x], {x, L1, L}] +
    A/(L II) Integrate[
      psi1'[x]*D[
        A11 Sinh[s1 x] + B11 Cosh[s1 x] + C11 Sin[s2 x] + D11 Cos[s2 x], {x,
         1}], {x, 0, L1}] +
    A/(L II) Integrate[
      psi2'[x]*D[
        A22 Sinh[s1 x] + B22 Cosh[s1 x] + C22 Sin[s2 x] + D22 Cos[s2 x], {x,
         1}], {x, L1, L}] == 0;
meqn10 = E22 (beta + A/(L II) Integrate[psi2'[x]*psi2'''[x], {x, L1, L}]) +
    E11 A/(L II)  Integrate[psi1'[x]*psi1'''[x], {x, 0, L1}] +
    A/(L II) Integrate[
      psi1'[x]*
       D[A11 Sinh[s1 x] + B11 Cosh[s1 x] + C11 Sin[s2 x] + D11 Cos[s2 x], {x,
         1}], {x, 0, L1}] +
    A/(L II) Integrate[
      psi2'[x]*D[
        A22 Sinh[s1 x] + B22 Cosh[s1 x] + C22 Sin[s2 x] + D22 Cos[s2 x], {x,
         1}], {x, L1, L}] == 0;
mat = CoefficientArrays[{meqn1, meqn2, meqn3, meqn4, meqn5, meqn6, meqn7,
     meqn8, meqn9, meqn10}, {A11, B11, C11, D11, E11, A22, B22, C22, D22,
     E22}][[2]];
MatrixRank[mat];
matrank = mat;
mateqn = {matrank[[1, All]]};
mattrial = mateqn;
count = 0;
For[ii = 2, ii <= Dimensions[matrank][[1]], ii++,
  mattrial = Join[mattrial, {matrank[[ii, All]]}];
  If[MatrixRank[mattrial] + count == ii,
   mateqn = Join[mateqn, {matrank[[ii, All]]}], {count = count + 1,
    mateqn = mateqn}];
  ];
eqnfrommat = mateqn.{A11, B11, C11, D11, E11, A22, B22, C22, D22, E22};
eqns1 = {eqnfrommat[[1]] == 0, eqnfrommat[[2]] == 0, eqnfrommat[[3]] == 0,
   eqnfrommat[[4]] == 0, eqnfrommat[[5]] == 0, eqnfrommat[[6]] == 0,
   eqnfrommat[[7]] == 0, eqnfrommat[[8]], eqnfrommat[[9]]};
sol = Flatten[NSolve[eqns1, {B11, C11, D11, E11, A22, B22, C22, D22, E22}]] //
```

```
    Chop;

B11a = B11 /. sol;
C11a = C11 /. sol;
D11a = D11 /. sol;
E11a = E11 /. sol;
A22a = A22 /. sol;
B22a = B22 /. sol;
C22a = C22 /. sol;
D22a = D22 /. sol;
E22a = E22 /. sol;
phi1[x_] =
  phi1[x] /. {B11 -> B11a, C11 -> C11a, D11 -> D11a, E11 -> E11a, A22 -> A22a,
     B22 -> B22a, C22 -> C22a, D22 -> D22a, E22 -> E22a};
phi2[x_] =
  phi2[x] /. {B11 -> B11a, C11 -> C11a, D11 -> D11a, E11 -> E11a, A22 -> A22a,
     B22 -> B22a, C22 -> C22a, D22 -> D22a, E22 -> E22a};
phitot[x_] = If[x <= L1, phi1[x], phi2[x]];

A11a = -1;


phi1[x_] = phi1[x] /. A11 -> A11a;
phi2[x_] = phi2[x] /. A11 -> A11a;
phitot[x_] = If[x <= L1, phi1[x], phi2[x]];

Plot[phitot[x], {x, 0, L}];




M1 = rho A NIntegrate[phi1[x]^2, {x, 0, L1}] +
   rho A NIntegrate[phi2[x]^2, {x, L1, L}] + M phi1[L1]^2;

MZ = rho A NIntegrate[phi1[x], {x, 0, L1}] +
   rho A NIntegrate[phi2[x], {x, L1, L}] + M phi1[L1];

KL = EE II NIntegrate[phitot''[x]^2, {x, 0, L}] -
   p NIntegrate[phitot'[x]^2, {x, 0, L}] +
   (EE A)/L NIntegrate[psitot'[x] phitot'[x], {x, 0, L}] NIntegrate[
     psitot'[x] phitot'[x], {x, 0, L}] +
   (EE A)/(2 L)
     NIntegrate[psitot'[x]^2, {x, 0, L}] NIntegrate[
     phitot'[x] phitot'[x], {x, 0, L}];


KQ = (EE A)/(2 L)
     NIntegrate[phitot'[x] phitot'[x], {x, 0, L}] NIntegrate[
     psitot'[x] phitot'[x], {x, 0, L}] + (EE A)/
    L NIntegrate[psitot'[x] phitot'[x], {x, 0, L}] NIntegrate[
     phitot'[x] phitot'[x], {x, 0, L}];
KQ1 = (3 EE A)/(2 L)
    NIntegrate[phitot'[x] phitot'[x], {x, 0, L}] NIntegrate[
    psitot'[x] phitot'[x], {x, 0, L}];

KC = (EE A)/(2 L)
    NIntegrate[phitot'[x] phitot'[x], {x, 0, L}] NIntegrate[
```

```
    phitot'[x] phitot'[x], {x, 0, L}];

solequil = Flatten[NSolve[KL x + KQ x^2 + KC x^3 == 0, x]];

botsol = x /. solequil[[1]] // Chop;
midsol = x /. solequil[[2]] // Chop;
topsol = x /. solequil[[3]] // Chop;



bottom = psitot[L1] + phitot[L1]*botsol;
middle = psitot[L1] + phitot[L1]*midsol;
top = psitot[L1] + phitot[L1]*topsol;

Print["bottom: ", bottom];
Print["middle: ", middle];
Print["top: ", top];

AppendTo[bottomvec, bottom];
AppendTo[middlevec, middle];
AppendTo[topvec, top];


equilvec = {botsol, midsol, topsol};
soljacobianvec = ConstantArray[0, Length[solequil]];


For[iii = 1, iii <= Length[solequil], iii++,
  jacobian = ( {
      {-\[Lambda]1, 1},
      {-KL/M1 - (2 KQ)/M1 xx1 - (3 KC)/M1 xx1^2, -\[Lambda]1}
     } ) /. xx1 -> equilvec[[iii]];
  soljacobian = Flatten[Solve[Det[jacobian] == 0, \[Lambda]1]] // Simplify;
  soljacobianvec[[iii]] = Flatten[soljacobian];
  lambdavec = {};
  For[jjj = 1, jjj <= Length[soljacobianvec[[iii]]], jjj++,
   AppendTo[lambdavec, \[Lambda]1 /. soljacobianvec[[iii, jjj]]];
   ];
  stablecheck = 0;
  For[jjj = 1, jjj <= Length[lambdavec], jjj++,
   If[Im[lambdavec[[jjj]]] != 0, stablecheck = stablecheck + 1];
   ];
  If[stablecheck == 2, {stableequil[[iii, jj]] = equilvec[[iii]],
    stableconfig[[iii, jj]] =
     psitot[L1] + phitot[L1]*stableequil[[iii, jj]]}, {unstableequil[[iii,
      jj]] = equilvec[[iii]],
    unstableconfig[[iii, jj]] =
     psitot[L1] + phitot[L1]*unstableequil[[iii, jj]]}];

  ];

botapprox[x_] = psitot[x] + phitot[x] * botsol;
midapprox[x_] = psitot[x] + phitot[x] * midsol;
topapprox[x_] = psitot[x] + phitot[x] * topsol;

Plot[{botapprox[x], midapprox[x], topapprox[x], -psitot[x], 0, psitot[x]}, {x,
   0, L}, PlotStyle -> {{Blue, Dashed}, {Red, Dashed}, {Green, Dashed}, Blue,
   Red, Green}, ImageSize -> Large, Frame -> True,
```

```
 FrameStyle -> Directive[Thick, Black, Bold], GridLines -> Automatic,
 FrameTicksStyle -> Black, FrameLabel -> {"Position (m)", "Beam Profile (m)"},
  LabelStyle -> Directive[Bold, Black, FontSize -> 18],
 PlotLegends ->
  Placed[LineLegend[{Style["bot approx", 11], Style["mid approx", 11],
     Style["top approx", 11], Style["bot exact", 11], Style["mid exact", 11],
     Style["top exact", 11]}, Spacings -> 0.15], {0.13, 0.83}]]

g = 9.81;

amp = 4.56;


f = 38;

tbeg = 0.78;
tfinal = 1;


c = 95;
D1 = c NIntegrate[phi1[x]^2, {x, 0, L1}] + c NIntegrate[phi2[x]^2, {x, L1, L}];


ep0 = 8.85*^-12;
epr = 2.5;
S = Lm*bm;

sigma = 125*^-7;
R = 10*^6;
di = psitot[L1];
T = 320*^-6;

gi = botapprox[L1] - 10*^-6;


ki = 30000;
ci = 3000;


base[t_] =
  Piecewise[{{0, t > 0 && t < tbeg}, {amp*g*Sin[f 2 Pi (t - tbeg)],
     t >= tbeg && t <= tbeg + 1/f 1/2}, {0, t > tbeg + 1/f 1/2}}];


diffeq = M1 u''[t] + MZ base[t] + KL u[t] + KQ u[t]^2 + KC u[t]^3 + D1 u'[t] +
    phi1[L1]/(2 ep0 S) q[t]^2 - (sigma phi1[L1])/ep0 q[t];


diffeqimpact =
  M1 u''[t] + MZ base[t] + ci u'[t] + ki u[t] + ki gi + KQ gi^2 + KC gi^3 +
   phi1[L1]/(2 ep0 S) q[t]^2 - (sigma phi1[L1])/ep0 q[t];

diffeqelectrical =
  q'[t] + 1/(ep0 R S) (T/epr + di + psitot[L1] + phi1[L1] u[t]) q[t] - (
    sigma (di + psitot[L1] + phi1[L1] u[t]))/(ep0 R) == 0;


diffeqtotal =
```

```
  Piecewise[{{diffeq, psi1[L1] + phi1[L1] u[t] > gi}, {diffeqimpact,
      psi1[L1] + phi1[L1] u[t] <= gi}}] == 0;


ndsol = Flatten[
   NDSolve[{diffeqtotal, diffeqelectrical, u[0] == 0, u'[0] == 0,
     q[0] == 0.0000}, {u[t], q[t]}, {t, 0, tfinal},
    InterpolationOrder -> All]];

U[t_] = u[t] /. ndsol;
Q[t_] = q[t] /. ndsol;



Plot[{U[t]*phi1[L1] + psi1[L1], botapprox[L1]*1}, {t, 0, tfinal},
 PlotRange -> {{0, tfinal}, {botapprox[L1]*1.1, topapprox[L1]*1.1}},
 ImageSize -> Large, Frame -> True,
 FrameStyle -> Directive[Thick, Black, Bold], FrameTicksStyle -> Black,
 FrameLabel -> {"Time (s)", "Beam Midspan Deflection (m)"},
 PlotLabel -> "Buckled Beam Under Shock",
 LabelStyle -> Directive[Bold, Black, FontSize -> 14]]



Plot[U'[t]*phi1[L1], {t, 0, tfinal}, PlotRange -> {{0, tfinal}, All},
 ImageSize -> Large, Frame -> True,
 FrameStyle -> Directive[Thick, Black, Bold], FrameTicksStyle -> Black,
 FrameLabel -> {"Time (s)", "Beam Midspan Velocity (m/s)"},
 PlotLabel -> "Buckled Beam Under Shock",
 LabelStyle -> Directive[Bold, Black, FontSize -> 14]]


Plot[Q'[t] R, {t, 0, tfinal}, PlotRange -> {{0, tfinal}, {-50, 50}},
 ImageSize -> Large, Frame -> True,
 FrameStyle -> Directive[Thick, Black, Bold], FrameTicksStyle -> Black,
 FrameLabel -> {"Time (s)", "Voltage Generated (V)"},
 PlotLabel -> "Buckled Beam Under Shock",
 LabelStyle -> Directive[Bold, Black, FontSize -> 14], GridLines -> Automatic]




(*voltdata=Import["tek0016.mat"];
voltdata=Import["tek0014.mat"];
voltdata=Import["tek0024.mat"];
voltdata=Import["tek0032.mat"];*)

SetDirectory[NotebookDirectory[]]
voltdata = Import["tek0032.mat"];
timevolt = voltdata[[1, All, 1]];
volt = voltdata[[2, All, 1]];
plotexpvoltg2 =
 ListLinePlot[Transpose[{timevolt, volt}], PlotRange -> {All, {-50, 50}},
  PlotStyle -> Red, ImageSize -> Large, Frame -> True,
  FrameStyle -> Directive[Thick, Black, Bold], FrameTicksStyle -> Black,
  FrameLabel -> {"Time (s)", "Voltage Generated (V)"},
  LabelStyle -> Directive[Bold, Black, FontSize -> 20],
  GridLines -> Automatic]
```

```
(*acceldata=Import["accel2p95.mat"];
acceldata=Import["accel3p26.mat"];
acceldata=Import["accel3p88.mat"];
acceldata=Import["accel4p56.mat"];*)

acceldata = Import["accel4p56.mat"];
timeaccel = acceldata[[2, All, 1]];
accel = acceldata[[1, All, 1]];
plotaccel =
 ListLinePlot[Transpose[{timeaccel, accel}], PlotRange -> {All, {-8, 8}},
  PlotStyle -> Red, ImageSize -> Large, Frame -> True,
  FrameStyle -> Directive[Thick, Black, Bold], FrameTicksStyle -> Black,
  FrameLabel -> {"Time (s)", "Base Acceleration (g)"},
  LabelStyle -> Directive[Bold, Black, FontSize -> 20],
  GridLines -> Automatic]

plotsimvoltg2 =
 Plot[Q'[t] R, {t, 0, tfinal}, PlotRange -> {{0, tfinal}, {-50, 50}},
  ImageSize -> Large, Frame -> True,
  FrameStyle -> Directive[Thick, Black, Bold], FrameTicksStyle -> Black,
  FrameLabel -> {"Time (s)", "Voltage Generated (V)"},
  LabelStyle -> Directive[Bold, Black, FontSize -> 20], PlotStyle -> Blue,
  GridLines -> Automatic]

Show[plotsimvoltg2, plotexpvoltg2]

accelvsvolt = Import["accelvsvolt.mat"];
accelvoltdata =
  Transpose[{accelvsvolt[[1, 1, All]], accelvsvolt[[2, 1, All]]}];
ListPlot[accelvoltdata, PlotRange -> {All, All}, PlotStyle -> Black,
 ImageSize -> Large, Frame -> True,
 FrameStyle -> Directive[Thick, Black, Bold], FrameTicksStyle -> Black,
 FrameLabel -> {"Base Acceleration (g)", "Voltage Generated (V)"},
 LabelStyle -> Directive[Bold, Black, FontSize -> 18], GridLines -> Automatic,
  PlotMarkers -> {Automatic, 15}]

posZoomIn =
  Plot[{(U[t]*phi1[L1] + psi1[L1])*1000, botapprox[L1]*1000}, {t, 0, tfinal},
   PlotRange -> {{0.7, 0.9}, {-2, 2}}, ImageSize -> Large,
   Frame -> {True, True, True, False},
   FrameStyle -> {{Thick, Automatic}, {Thick, Blue}, {Thick,
      Automatic}, {Thick, Automatic}},
   FrameLabel -> {"Time (s)", "Beam Midspan Deflection (mm)"},
   LabelStyle -> Directive[Bold, Black, FontSize -> 18], ImagePadding -> 70,
   PlotStyle -> {Blue, Green}, GridLines -> Automatic];

velZoomIn =
  Plot[{(U'[t]*phi1[L1] + psi1[L1])*1000}, {t, 0, tfinal},
   PlotRange -> {{0.7, 0.9}, All}, ImageSize -> Large,
   Frame -> {False, False, False, True},
   FrameTicks -> {{None, All}, {None, None}},
   FrameStyle -> {{Thick, Automatic}, {Thick, Automatic}, {Thick,
      Automatic}, {Thick, Red}},
   FrameLabel -> {{None, "Beam Midspan Velocity (mm/s)"}, {None, None}},
   LabelStyle -> Directive[Bold, Black, FontSize -> 18], ImagePadding -> 70,
   PlotStyle -> {Red}, Axes -> True, GridLines -> Automatic];
Overlay[{posZoomIn, velZoomIn}]
```

```
SetDirectory[NotebookDirectory[]]
(*Export["pos_vel_zoom_in.eps",Overlay[{posZoomIn,velZoomIn}]]*)

chargeZoomIn =
  Plot[{Q[t]*1*^9}, {t, 0, tfinal}, PlotRange -> {{0.75, 0.85}, All},
   ImageSize -> Large, Frame -> {True, True, True, False},
   FrameStyle -> {{Thick, Automatic}, {Thick, Blue}, {Thick,
      Automatic}, {Thick, Automatic}},
   FrameLabel -> {"Time (s)", "Charge transferred (GC)"},
   LabelStyle -> Directive[Bold, Black, FontSize -> 18], ImagePadding -> 70,
   PlotStyle -> {Blue}, GridLines -> Automatic];

voltZoomIn =
  Plot[{Q'[t] R}, {t, 0, tfinal}, PlotRange -> {{0.75, 0.85}, {-50, 20}},
   ImageSize -> Large, Frame -> {False, False, False, True},
   FrameTicks -> {{None, All}, {None, None}},
   FrameStyle -> {{Thick, Automatic}, {Thick, Automatic}, {Thick,
      Automatic}, {Thick, Red}},
   FrameLabel -> {{None, "Voltage (V)"}, {None, None}},
   LabelStyle -> Directive[Bold, Black, FontSize -> 18], ImagePadding -> 70,
   PlotStyle -> {Red}, Axes -> True, GridLines -> Automatic];
Overlay[{chargeZoomIn, voltZoomIn}]
(*Export["charge_volt_zoom_in.eps",Overlay[{chargeZoomIn,voltZoomIn}]]*)
```

References

[1] Zhong Lin Wang. Triboelectric nanogenerators as new energy technology and self-powered sensors–principles, problems and perspectives. *Faraday discussions*, 176:447–458, 2015.

[2] Michael W Shafer, Robert MacCurdy, J Ryan Shipley, David Winkler, Christopher G Guglielmo, and Ephrahim Garcia. The case for energy harvesting on wildlife in flight. *Smart Materials and Structures*, 24(2):025031, 2015.

[3] KA Cook-Chennault, N Thambi, and AM Sastry. Powering mems portable devicesa review of non-regenerative and regenerative power supply systems with special emphasis on piezoelectric energy harvesting systems. *Smart Materials and Structures*, 17(4):043001, 2008.

[4] Cian Ó Mathúna, Terence ODonnell, Rafael V Martinez-Catala, James Rohan, and Brendan OFlynn. Energy scavenging for long-term deployable wireless sensor networks. *Talanta*, 75(3):613–623, 2008.

[5] Jens Twiefel and Henrik Westermann. Survey on broadband techniques for vibration energy harvesting. *Journal of Intelligent Material Systems and Structures*, 24(11):1291–1302, 2013.

[6] Alwathiqbellah Ibrahim, Shahrzad Towfighian, and Mohammad I Younis. Dynamics of transition regime in bistable vibration energy harvesters. *Journal of Vibration and Acoustics*, 139(5):051008, 2017.

[7] BP Mann and ND Sims. Energy harvesting from the nonlinear oscillations of magnetic levitation. *Journal of Sound and Vibration*, 319(1):515–530, 2009.

[8] Ravindra Masana and Mohammed F Daqaq. Electromechanical modeling and nonlinear analysis of axially loaded energy harvesters. *Journal of Vibration and Acoustics*, 133(1):011007, 2011.

[9] AJ Sneller, P Cette, and BP Mann. Experimental investigation of a post-buckled piezoelectric beam with an attached central mass used to harvest energy. *Proceedings of the Institution of Mechanical Engineers, Part I: Journal of Systems and Control Engineering*, 225(4):497–509, 2011.

[10] Li-Qun Chen and Wen-An Jiang. Internal resonance energy harvesting. *Journal of Applied Mechanics*, 82(3):031004–031004–11, Mar 2015. ISSN 0021-8936.

[11] Wei Yang and Shahrzad Towfighian. Internal resonance and low frequency vibration energy harvesting. *Smart Materials and Structures*, 26(9):095008, 2017.

[12] Alwathiqbellah Ibrahim, Abdallah Ramini, and Shahrzad Towfighian. Experimental and theoretical investigation of an impact vibration harvester with triboelectric transduction. *Journal of Sound and Vibration*, 416:111–124, 2018.

[13] M. A. E. Mahmoud, E. M. Abdel-Rahmany, E. F. El-Saadany, and R. R. Mansour. Battery-less electrostatic micro-power generator. In *2009 2nd Microsystems and Nanoelectronics Research Conference*, pages 29–32, Oct 2009.

[14] M. Soliman, E. Abdel-Rahman, E. F. El-Saadany, and R. R. Mansour. A design procedure for wideband micropower generators. *Journal of Microelectromechanical Systems*, 18:1288–1299, 2009.

[15] Shad Roundy and Yang Zhang. Toward self-tuning adaptive vibration-based microgenerators. In *Smart Materials, Nano-, and Micro-Smart Systems*, pages 373–384. International Society for Optics and Photonics, 2005.

[16] Wen-Jong Wu, Yu-Yin Chen, Bor-Shun Lee, Jyun-Jhang He, and Yen-Tun Peng. Tunable resonant frequency power harvesting devices. In *Smart Structures and Materials*, pages 61690A–61690A. International Society for Optics and Photonics, 2006.

[17] SM Shahruz. Design of mechanical band-pass filters for energy scavenging. *Journal of Sound and Vibration*, 292(3):987–998, 2006.

[18] Eli S Leland and Paul K Wright. Resonance tuning of piezoelectric vibration energy scavenging generators using compressive axial preload. *Smart Materials and Structures*, 15(5):1413, 2006.

[19] Dylan J Morris, John M Youngsman, Michael J Anderson, and David F Bahr. A resonant frequency tunable, extensional mode piezoelectric vibration harvesting mechanism. *Smart Materials and Structures*, 17(6):065021, 2008.

[20] George A Lesieutre and Christopher L Davis. Can a coupling coefficient of a piezoelectric device be higher than those of its active material? *Journal of intelligent material systems and structures*, 8(10):859–867, 1997.

[21] Mohammed F Daqaq. Response of uni-modal duffing-type harvesters to random forced excitations. *Journal of Sound and Vibration*, 329(18):3621–3631, 2010.

[22] Son D Nguyen, Einar Halvorsen, and Igor Paprotny. Bistable springs for wideband microelectromechanical energy harvesters. *Applied Physics Letters*, 102(2):023904, 2013.

[23] Ravindra Masana and Mohammed F Daqaq. Relative performance of a vibratory energy harvester in mono-and bi-stable potentials. *Journal of Sound and Vibration*, 330(24):6036–6052, 2011.

[24] Feng-Ru Fan, Zhong-Qun Tian, and Zhong Lin Wang. Flexible triboelectric generator. *Nano Energy*, 1(2):328–334, 2012.

[25] Zhong Lin Wang. Triboelectric nanogenerators as new energy technology for self-powered systems and as active mechanical and chemical sensors. *ACS nano*, 7(11):9533–9557, 2013.

[26] A. Narimani, M. E. Golnaraghi, and G. Nakhaie Jazar. Frequency response of a piecewise linear vibration isolator. *Modal Analysis*, 10(12):1775–1794, 2004.

[27] M.I. Younis. *MEMS Linear and Nonlinear Statics and Dynamics*. Microsystems. Springer US, 2011. ISBN 9781441960207.

[28] Guangyi Shi, Cheung-Shing Chan, Guanglie Zhang, Wen J Li, Philip HW Leong, and Kwok-Sui Leung. Towards a mobile airbag system using mems sensors and embedded intelligence. In *Robotics and Biomimetics, 2007. ROBIO 2007. IEEE International Conference on*, pages 634–639, 2007.

[29] Jeung Sang Go, Young Ho Cho, Byung Man Kwak, and Kwanhum Park. Snapping microswitches with adjustable acceleration threshold. *Sensors and Actuators, A: Physical*, 54(1-3):579–583, 1996. ISSN 09244247.

[30] Jian Zhao, Jianyuan Jia, Hongxi Wang, and Wanli Li. A novel threshold accelerometer with postbuckling structures for airbag restraint systems. *IEEE Sensors Journal*, 7(8):1102–1109, 2007. ISSN 1530437X.

[31] Abdallah Ramini, Mohammad I Younis, and Quang T Su. A low-g electrostatically actuated resonant switch. *Smart Materials and Structures*, 22(2): 025006, 2012.

[32] Sven Michaelis, Hans Jörg Timme, Michael Wycisk, and Josef Binder. Additive electroplating technology as a post-CMOS process for the production of MEMS acceleration-threshold switches for transportation applications. *Journal of Micromechanics and Microengineering*, 10(2):120–123, 2000. ISSN 09601317.

[33] Tadao Matsunaga and Masayoshi Esashi. Acceleration switch with extended holding time using squeeze film effect for side airbag systems. *Sensors and Actuators, A: Physical*, 100(1):10–17, 2002. ISSN 09244247. doi: 10.1016/S0924-4247(02)00039-0.

[34] L. Zimmermann, J.Ph. Ebersohl, F. Le Hung, J.P. Berry, F. Baillieu, P. Rey, B. Diem, S. Renard, and P. Caillat. Airbag application: a microsystem including a silicon capacitive accelerometer, cmos switched capacitor electronics and true self-test capability. *Sensors and Actuators A: Physical*, 46(1):190 – 195, 1995. ISSN 0924-4247.

[35] Inventors Douglas A Woodman and R Michael. United States Patent (19). (19), 1991.

[36] H Gleason. 32.4%-4%. pages 2–7, 1953.

[37] Alwathiqbellah Ibrahim and Mohammad I. Younis. Simple fall criteria for MEMS sensors: Data analysis and sensor concept. *Sensors (Switzerland)*, 14 (7):12149–12173, 2014. ISSN 14248220.

[38] Luke J Currano, Scott Bauman, Wayne Churaman, Marty Peckerar, James Wienke, Seokjin Kim, Miao Yu, and Balakumar Balachandran. Latching ultra-low power mems shock sensors for acceleration monitoring. *Sensors and Actuators A: Physical*, 147(2):490–497, 2008.

[39] Luke J Currano, Miao Yu, and Balakumar Balachandran. Latching in a mems shock sensor: Modeling and experiments. *Sensors and Actuators A: Physical*, 159(1):41–50, 2010.

[40] Il-Han Hwang, Yu-Seok Shim, and Jong-Hyun Lee. Modeling and experimental characterization of the chevron-type bi-stable microactuator. *Journal of Micromechanics and Microengineering*, 13(6):948, 2003.

[41] Jasmina Casals-Terre and Andrei Shkel. Dynamic analysis of a snap-action micromechanism. In *Sensors, 2004. Proceedings of IEEE*, pages 1245–1248. IEEE, 2004.

[42] Ho Nam Kwon, Il-Han Hwang, and Jong-Hyun Lee. A pulse-operating electrostatic microactuator for bi-stable latching. *Journal of Micromechanics and Microengineering*, 15(8):1511, 2005.

[43] Slava Krylov, Bojan R Ilic, David Schreiber, Shimon Seretensky, and Harold Craighead. The pull-in behavior of electrostatically actuated bistable microstructures. *Journal of Micromechanics and Microengineering*, 18(5): 055026, 2008.

[44] Jin Qiu, Jeffrey H Lang, Alexander H Slocum, and Alexis C Weber. A bulk-micromachined bistable relay with u-shaped thermal actuators. *Journal of Microelectromechanical Systems*, 14(5):1099–1109, 2005.

[45] Daniel L Wilcox and Larry L Howell. Fully compliant tensural bistable micromechanisms (ftbm). *Journal of Microelectromechanical Systems*, 14(6): 1223–1235, 2005.

[46] Yao-Joe Yang, Bo-Ting Liao, and Wen-Cheng Kuo. A novel 2× 2 mems optical switch using the split cross-bar design. *Journal of Micromechanics and Microengineering*, 17(5):875, 2007.

[47] Michihito Ueda, Yukihiro Kaneko, Yu Nishitani, and Atsushi Omote. Battery-less shock-recording device consisting of a piezoelectric sensor and a ferroelectric-gate field-effect transistor. *Sensors and Actuators A: Physical*, 232:75 – 83, 2015. ISSN 0924-4247.

[48] Georgios Giannopoulos, Javier Monreal, and John Vantomme. Snap-through buckling behavior of piezoelectric bimorph beams: I. analytical and numerical modeling. *Smart materials and structures*, 16(4):1148, 2007.

[49] Hee-Chul Lee, Jae-Hyoung Park, Jae-Yeong Park, Hyo-Jin Nam, and Jong-Uk Bu. Design, fabrication and rf performances of two different types of piezoelectrically actuated ohmic mems switches. *Journal of micromechanics and microengineering*, 15(11):2098, 2005.

[50] Jae-Hyoung Park, Hee-Chul Lee, Yong-Hee Park, Yong-Dae Kim, Chang-Hyeon Ji, Jonguk Bu, and Hyo-Jin Nam. A fully wafer-level packaged rf mems switch with low actuation voltage using a piezoelectric actuator. *Journal of Micromechanics and Microengineering*, 16(11):2281, 2006.

[51] SJ Gross, S Tadigadapa, TN Jackson, S Trolier-McKinstry, and QQ Zhang. Lead-zirconate-titanate-based piezoelectric micromachined switch. *Applied Physics Letters*, 83(1):174–176, 2003.

[52] Ronald G. Polcawich, Jeffrey S. Pulskamp, Daniel Judy, Prashant Ranade, Susan Trolier-McKinstry, and Madan Dubey. Surface Micromachined Microelectromechancial Ohmic Series Switch Using Thin-Film Piezoelectric Actuators. *IEEE Transactions on Microwave Theory and Techniques*, 55(12): 2642–2654, 2007. ISSN 15579670.

[53] Marc Sulfridge, Taher Saif, Norman Miller, and Keith O'Hara. Optical actuation of a bistable mems. *Journal of microelectromechanical systems*, 11(5): 574–583, 2002.

[54] Jong Soo Ko, Min Gon Lee, Jeong Sam Han, Jeung Sang Go, Bosung Shin, and Dae-Sik Lee. A laterally-driven bistable electromagnetic microrelay. *ETRI journal*, 28(3):389–392, 2006.

[55] Andrew Cao, Jongbaeg Kim, and Liwei Lin. Bi-directional electrothermal electromagnetic actuators. *Journal of Micromechanics and Microengineering*, 17(5):975, 2007.

[56] Jasmina Casals-Terre, Andreu Fargas-Marques, and Andrei M Shkel. Snap-action bistable micromechanisms actuated by nonlinear resonance. *Journal of microelectromechanical systems*, 17(5):1082–1093, 2008.

[57] W Kreider and Ali H Nayfeh. Experimental investigation of single-mode responses in a fixed-fixed buckled beam. *Nonlinear Dynamics*, 15(2):155–177, 1998.

[58] K Das and RC Batra. Pull-in and snap-through instabilities in transient deformations of microelectromechanical systems. *Journal of Micromechanics and Microengineering*, 19(3):035008, 2009.

[59] Mattias Vangbo. An analytical analysis of a compressed bistable buckled beam. *Sensors and Actuators, A: Physical*, 69(3):212–216, 1998. ISSN 09244247.

[60] Jen-San Chen and Jian-San Lin. Exact Critical Loads for a Pinned Half-Sine Arch Under End Couples. *Journal of Applied Mechanics*, 72(1):147, 2005. ISSN 00218936.

[61] C Robinson, D Overman, R Warner, and T Blomqulst. Problems encountered in the development of a microscale g-switch using three design approaches. In *Proc. Int. Conf. on Solid-State Sensors and Actuators, Tokyo, Japan*, pages 410–413, 1987.

[62] Y Loke, GH McKinnon, and MJ Brett. Fabrication and characterization of silicon micromachined threshold accelerometers. *Sensors and Actuators A: Physical*, 29(3):235–240, 1991.

[63] T. Tønnesen, O. Lüdtke, J. Noetzel, J. Binder, and G. Mader. Simulation, design and fabrication of electroplated acceleration switches. *Journal of Micromechanics and Microengineering*, 7(3):237–239, 1997. ISSN 09601317.

[64] PF Man and CH Mastrangelo. Surface micromachined shock sensor for impact detection. In *Solid-State Sensor and Actuato Workshop (Hilton Head)*, pages 156–9, 1994.

[65] Chi Zhang, Tao Zhou, Wei Tang, Changbao Han, Limin Zhang, and Zhong Lin Wang. Rotating-disk-based direct-current triboelectric nanogenerator. *Advanced Energy Materials*, 4(9), 2014.

[66] Ali Hasan Nayfeh and P. Frank Pai. *Linear and nonlinear structural mechanics*. New York ; Chichester : Wiley, 2004. ISBN 0471593567. Formerly CIP.

[67] Samir A. Emam. *A theoretical and experimental study of nonlinear dynamics of buckled beams*. dissertation, Virginia Polytechnic Institute and State University, 2002.